


Dynamics of monopile-supported offshore wind turbines under ship impact loading: a generalised frequency domain approach

Somya Ranjan Patro ^{a*}, Arnab Banerjee^a, Sondipon Adhikari^b and G. V. Ramana^a

^aDepartment of Civil Engineering, Indian Institute of Technology Delhi, New Delhi, India; ^bJames Watt School of Engineering, University of Glasgow, Glasgow, UK

ABSTRACT

This study conducts the dynamic analysis of a monopile-supported offshore wind turbine (MSWT) under ship impact in frequency domain analysis. The approach utilises dynamic stiffness formulation to capture the force-displacement relationship of both the tower and the monopile. The tower and the monopile are modelled using the Euler-Bernoulli beam theory, where the exact solutions for the non-uniform geometry of the tower are obtained using Bessel function solutions. The effect of fluid-structure interaction (FSI) and the soil-structure interaction (SSI) is incorporated using the hydrodynamic mass and viscoelastic springs distributed along the length of the monopile. The study focuses on capturing the dynamic response at the tower top within the frequency domain when subjected to impact loading at its base. A parametric analysis investigates how this response varies concerning ship mass, impact velocity, and water depth. Further, a simplified non-dimensional model is proposed, accounting for the tower's non-uniformity and representing the foundation with lateral and rotational springs. Finally, an analytical, approximate, closed-form expression for natural frequency is developed, aiding in the preliminary design of beam-like structures with conical shapes and flexible supports. These analytical tools complement experiments and finite element studies, offering early insights into MSWT dynamics under impact. The proposed model effectively captures the dynamic response of MSWTs under varying impact energies and deformation modes from local indentations to global bending and incorporates foundation and geometric effects for diverse design scenarios.

ARTICLE HISTORY

Received 16 November 2024
Accepted 10 May 2025

KEYWORDS

Monopile-supported wind turbine; dynamic stiffness formulation; fluid-structure interaction; soil-structure interaction; Bessel function solution

Nomenclature

F_I	Impact force	θ_t	Slope component of the tower
M_R	Mass of the RNA	M_t	Bending moment component of the tower
H_s	Height of monopile embedded in soil	$(\bullet)^I$	Partial differential concerning spatial coordinate
A_t	Cross-sectional area of the tower	V_t	Shear force component of the tower
E_t	Young's modulus of the tower	\mathbf{D}	Displacement vector of the tower
I_t	Second moment of area of the tower	\mathbf{F}	Force vector of the tower
w_t	Transverse displacement of the tower	\mathbf{S}	Dynamic stiffness matrix of the tower
ρ_t	Density of the tower	k_s	Stiffness of the viscoelastic springs
H_t	Height of the tower	c_s	Damping of the viscoelastic springs
r_t	Top outer radius of the tower	w_s	Transverse displacement of the monopile embedded in soil
D_{tt}	Top outer diameter of the tower	W_s	Transverse displacement of the monopile embedded in soil as a function of co-ordinate axis only
r_b	Bottom outer radius of the tower	\mathbf{K}	Combined dynamic stiffness matrix considering the tower as well as the RNA
D_{tb}	Bottom outer diameter of the tower	E_p	Young's modulus of the monopile
R	Radius of the tower	I_p	Second moment of area of the monopile
τ	Thickness of the tower	ρ_p	Density of the monopile
i	Complex integer	A_p	Cross-sectional area of the monopile
$yota$		w_f	Transverse displacement of the monopile submerged in water
W_t	Transverse displacement of the tower as a function of co-ordinate axis only	W_f	Transverse displacement of the monopile submerged in water as a function of co-ordinate axis only
ω	Excitation frequency	x_f	Co-ordinate axis of monopile submerged in water
I_n	n th order modified Bessel functions of the first kind	θ_f	Slope component of monopile submerged in water
J_n	n th order Bessel functions of the first kind		
K_n	n th order modified Bessel functions of the second kind		
Y_n	n th order Bessel functions of the second kind		
A_j	j number of arbitrary constants corresponding to the transverse equations of motion of the tower		

H_f	Depth of the monopile submerged in water	\bar{w}	Non-dimensional form of transverse displacement of the tower
r_p	Outside radius of the monopile	\bar{W}	Non-dimensional form of transverse displacement of the tower as a function of co-ordinate axis only
ρ_w	Water density m Hydrodynamic mass, which represents the lateral resistance of the water-pile interface	$\bar{\omega}$	Arbitrary constants bearing the units of dimensional quantity η Frequency ratio
M_f	Bending moment component of monopile submerged in water	$\bar{\theta}$	Non-dimensional form of the slope component of the tower
V_f	Shear force component of monopile submerged in water	\bar{M}	Non-dimensional form of the bending moment component of the tower
C_l	l number of arbitrary constants corresponding to the transverse equations of motion of the monopile element submerged in water α Wave numbers of the monopile element submerged in water	\bar{V}	Non-dimensional form of the shear force component of the tower
D_f	Displacement vector of the monopile element submerged in water	K_L	Lateral spring stiffness coefficients
F_f	Force vector of the monopile element submerged in water	κ_L	Non-dimensional form of lateral spring stiffness coefficients
S_f	Dynamic stiffness matrix of the monopile element submerged in water	K_R	Rotational spring stiffness coefficients
D_G	Global displacement vector of the tower and monopile combined	κ_R	Non-dimensional form of rotational spring stiffness coefficients
F_G	Global force vector of the tower and monopile combined	S_t	Non-dimensional form of dynamic stiffness matrix of the tower ρ Density of PLA E Young's Modulus of PLA H Height of PLA tower D Outer diameter of PLA tower
S_G	Global dynamic stiffness matrix of the tower and monopile combined	τ_p	Thickness of PLA tower
x_s	Co-ordinate axis of monopile embedded in soil	M_r	Rigid Mass on top of PLA tower
θ_s	Slope component of monopile embedded in soil	M_a	Mass on accelerometer
M_s	Bending moment component of monopile embedded in soil	ω_e	Natural frequency from experiment
V_s	Shear force component of monopile embedded in soil	ω_b	Natural frequency from Bessel function solution
G_s	Shear modulus of the soil medium	ω_n	Natural frequency from Numerical simulation
μ_s	Poisson's ratio of the soil medium β Wave numbers of the monopile element embedded in soil	P_{ss}	Static load in the lateral direction at the top of the monopile
D_k	k number of arbitrary constants corresponding to the transverse equations of motion of the monopile element embedded in soil	P_s	Static load in lateral direction at the top of the tower δ Frequency ratio of the SDOF system
$S_{\bar{\omega}_x, \bar{\omega}_y}(\bar{\omega}, z)$	Spectral density of the turbulent gust drag force	M_{ss}	Static Moment
ρ_a	Air density	K_e	Equivalent stiffness of the SDOF system
$\bar{U}(z)$	Wind velocity	M_e	Equivalent mass of the SDOF system
A_T	Average cross-sectional area of the tower	ω_1	Natural frequency of the SDOF system
C_D	Drag coefficient of the wind turbine tower	γ_m	Mass correction factor
C_T	Thrust coefficient	γ_k	Stiffness correction factor
A_R	Cross-sectional area of the rotor χ Aerodynamic admittance	T_K	Kinetic energy
$S_{u_x, u_y}(\bar{\omega})$	Cross-power spectral density function of fluctuating wind speed	η_{rat}	Ratio of natural frequency of flexible support to that of fixed support
C_m	Inertia coefficient		
$S_{FF, waves}(\bar{\omega}, z_w)$	Power spectrum of the wave force exerted on the monopile		
D_P	Outer diameter of the monopile S Mean sea depth ψ Wave number		
$S_{ww}(\bar{\omega})$	Ocean wave		
R_M	Ratio of the mass of ship to the mass of MSWT		
R_H	Ratio of the height of monopile submerged in water to the total height of monopile		
R_V	Ratio of the impact velocity of the ship to the initial velocity of the ship		
M_S	Mass of the ship		
v_I	Impact velocity of the ship		
v_0	Initial velocity of the ship		
H_P	Total height of the monopile		
E_s	Young's modulus of the soil		
ρ_s	Density of the soil		
\bar{x}	Non-dimensional form of co-ordinate axis of the tower		
\bar{t}	Non-dimensional form of time		
\bar{c}	Non-dimensional form of conicity		

1. Introduction

Rapid industrialisation has significantly increased global energy demands, accelerating the depletion of non-renewable fossil fuel resources, such as coal and oil (Freedman 2024). This surge in energy consumption has concurrently driven a notable increase in CO₂ emissions, further exacerbating the challenges posed by climate change (Shah et al. 2024). The strategy to achieve the sustainable development goals (SDGs), particularly SDG7's objective of net-zero emissions by 2050, involves adopting renewable energy sources (Moreno et al. 2024). Among these, wind energy stands out as a leader due to its substantial production capacity and technological advancements (Ahmed et al. 2024). India, ranked as the fourth-largest global producer of wind energy, had exceeded 45 GW of production by January 2024, with projections surpassing 60 billion units (Musial et al. 2023). According to the National Electricity Plan of the central government for the period

ending 2032, India's installed wind capacity is estimated to reach approximately 73 GW in 2026–2027 and 122 GW by 2031–2032 (Anil Bindu and Thampatty 2024). In the late 1980s, wind turbines globally had a capacity of about 65 kW. Thanks to technological progress, today, wind turbines with 10 MW onshore and 15 MW offshore capacities are being successfully deployed worldwide (Qin et al. 2023). Investing in offshore wind turbines (OWTs) is motivated by higher average wind speeds at sea, reduced turbulence, wind shear, and the conservation of onshore resources (Liu et al. 2024). The design of OWT foundations primarily addresses the challenge of lateral forces, with monopile foundations being preferred for approximately 80% of installations (R. Das, Patro et al. 2024). The cost of these foundations constitutes about 34% of the total turbine investment (Pezeshki, Pavlou, Siriwardane et al. 2024).

The structural integrity of taller wind turbine towers, equipped with more powerful turbines and larger rotor

diameters, faces heightened external forces, including those from wind, waves, and seismic activities (Gücüyen 2017), as illustrated in Figure 1. Owing to their design and structural characteristics, OWTs are dynamically sensitive, as a significant rotating mass is mounted atop a long, slender column (James et al. 2024). Guided by the Limit State design philosophy, the structures must satisfy various limit states: Ultimate Limit State (ULS), Serviceability Limit State (SLS), Fatigue Limit State (FLS), and Accidental Limit State (ALS) (Bhattacharya 2019). With the increasing number of offshore wind installations near maritime traffic routes, the likelihood of collision events with drifting ships and approaching service vessels increases, raising safety concerns among regulatory bodies and project stakeholders (Ladeira, Márquez et al. 2023). At the turbine level, ensuring the crash-worthiness of the structure for a specified ALS requires structural analysts to employ a range of methodologies, typically based on non-linear finite element methods or

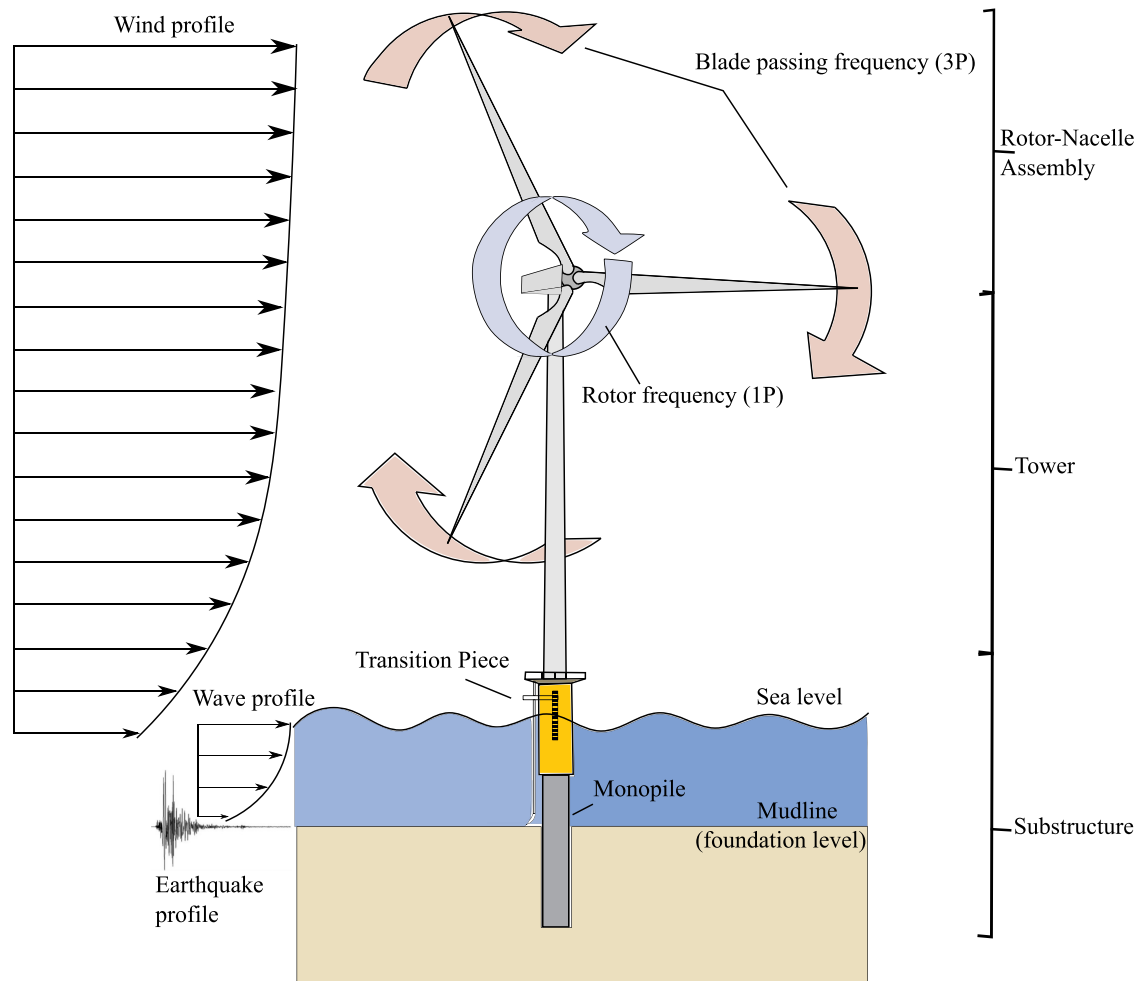


Figure 1. Various forces exert influence on a wind turbine supported by a monopile (MSWT) DNV GL AS Oslo (2016). (This figure is available in colour online.)

simplified analytical formulas, to assess potential damage and residual strength (Nie et al. 2024).

Minorsky (1958) was the first to investigate ship collisions in 1959 systematically. Later, Derucher (1982) converted the collision problem into an energy conversion problem, conceptualising the colliding object as part of a spring system. Building on this model, numerous researchers have examined various factors such as collision velocity, mass distribution above the tower, and water depth, to analyze the effects of ship impacts on different offshore wind turbine (OWT) foundations both analytically (Hsieh 2015; Le Sourné et al. 2016; Echeverry et al. 2017; Pire et al. 2018; Broersen 2020) and numerically (Bela et al. 2017; Hao and Liu 2017; Moulas et al. 2017; Gao and Zhang 2021; Zhang and Hu 2022). When an OWT is struck by a ship, it may experience local plastic indentation at the point of impact, leading to permanent deformations that weaken the tower's structural integrity (Mehreganian et al. 2024). The force of the collision can create a plastic hinge near the seabed due to excessive bending moments, potentially compromising stability (Ladeira, Jaramillo et al. 2023). Over time, cumulative damage from repeated impacts can initiate cracks and further reduce the turbine's load-bearing capacity, necessitating careful evaluation to prevent catastrophic failure (Moulas et al. 2017). These studies reveal that the dynamic response of the OWT reaches a peak at its resonant frequencies when subjected to ship impacts, making accurate determination of these frequencies crucial (Song et al. 2021). Moreover, the natural frequencies of the OWT system mustn't coincide with excitation frequencies – such as wind, wave, the rotational frequency of the rotor (1P), and the blade passing frequency of a three-bladed wind turbine (3P) – to prevent resonance and mitigate extensive fatigue damage (Wan et al. 2023). Figure 2 depicts three zones during the design phase, labelled soft-soft, soft-stiff, and stiff-stiff, around these

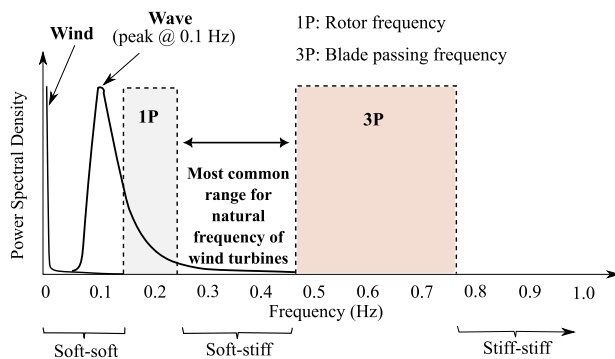


Figure 2. Frequency range of loads acting on wind turbines Ko (2020). (This figure is available in colour online.)

excitation frequencies (Arany et al. 2016). Thus, a vast body of literature employing both analytical (Arany, Bhattacharya, Adhikari et al. 2015; Darvishi-Alamouti et al. 2017; Ferreira et al. 2022; Pezeshki, Pavlou, Adeli et al. 2023; Yu and Amdahl 2023) and numerical methods (Ma et al. 2017; Bouzid et al. 2018; Bisoi and Haldar 2019; Alkhoury et al. 2021; Demirci et al. 2022) supports the estimation of natural frequencies in monopile-supported offshore wind turbines (MSWT).

Most of the methods mentioned previously either employ simplified analytical techniques or finite element methods (FEM) to estimate only the first natural frequency of the monopile-supported offshore wind turbine (MSWT) (Moynihan et al. 2023). In these methods, the tower and the monopile are primarily modelled using the Euler Bernoulli beam theory due to their high slenderness ratio (Norén-Cosgriff and Kaynia 2021). However, for larger OWTs, the natural frequency of the entire system is significantly reduced, activating multiple structural resonance frequencies during operation (Meng and Zhangqi 2011). Consequently, a comprehensive method that considers various natural frequencies and vibration modes is essential for reliable dynamic analysis (Gu et al. 2021). Although few researchers have considered Rayleigh–Ritz solutions to obtain multiple structural resonance frequencies, the accuracy of higher-order modes depends heavily on the choice of assumed basis functions (Yu and Amdahl 2023). This increases the computational complexity due to the coupling between bending and torsion. Despite these challenges, a few researchers have adopted the Spectral Element Matrix (SEM) or Dynamic Stiffness Matrix (DSM) approaches to determine eigenfrequencies (Kleusberg 2017; Adhikari and Bhattacharya 2021; Colherinhas et al. 2022). These frequency-domain approaches provide exact solutions to the governing equations of motion, adhering to appropriate boundary conditions (Wang K et al. 2017). A distinctive advantage of the DSM is its precise treatment of mass distribution within the elements, enabling accurate modelling of both the tower and the monopile (Lee 2009). Unlike methods that expand eigenfunctions, this approach bypasses the traditional FEM step of calculating natural frequencies and modal shapes, thus avoiding errors from series truncation (Leung 2012). Additionally, while the conventional analytical and numerical methods for assessing the dynamic response to OWT impacts rely on FEM or time-domain analysis, the importance of the frequency-domain approach, particularly for addressing resonance frequencies of the OWT, should not be underestimated (Jahani et al. 2022).

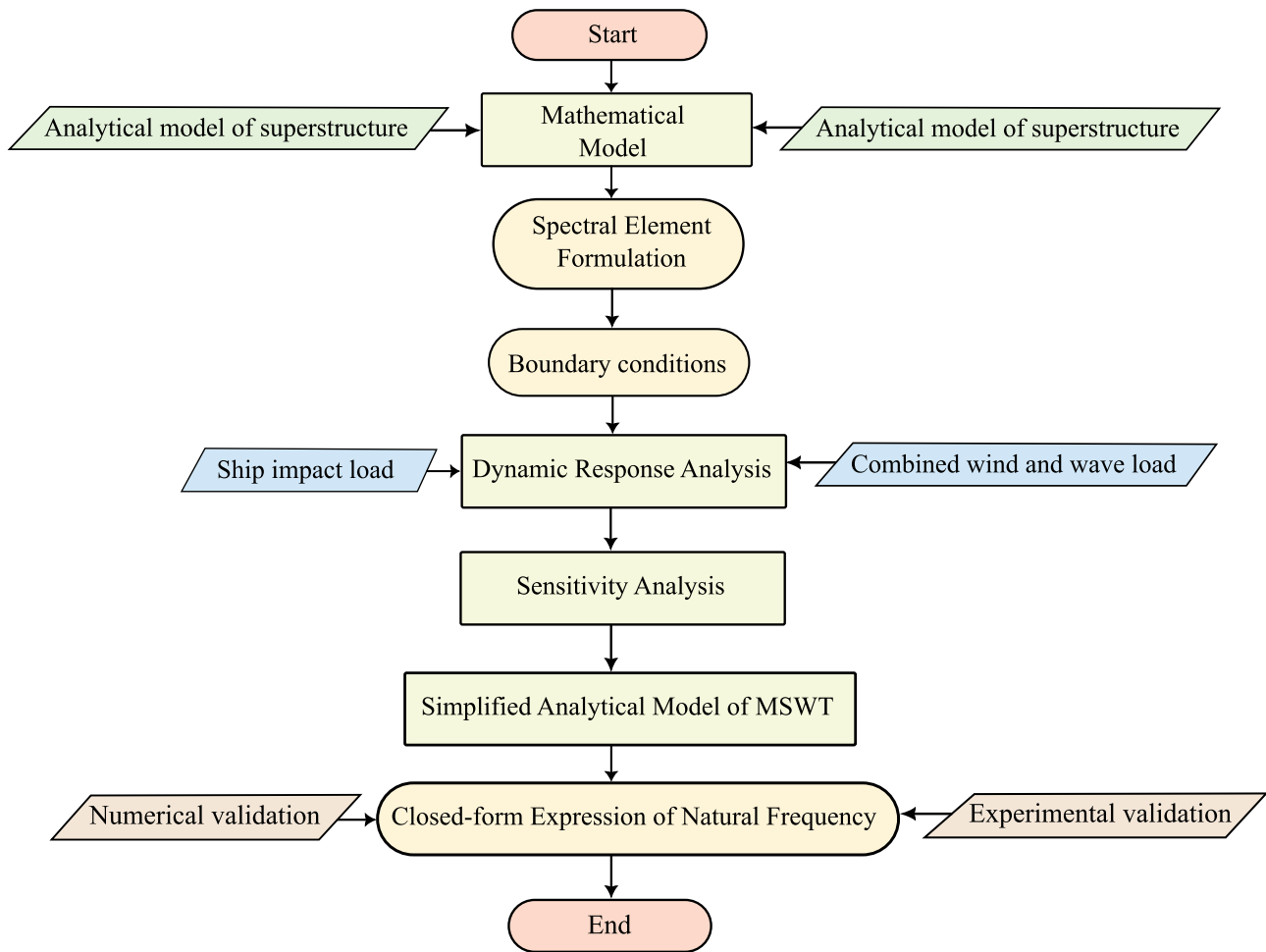


Figure 3. Flow chart of the present study. (This figure is available in colour online.)

In light of these limitations, the current study employs the DSM approach to establish the force-displacement relationship for the tower and monopile. A complete analytical methodology has been proposed for fluid-structure interaction (FSI) and soil-structure interaction (SSI). The FSI is incorporated through the hydrodynamic mass distributed along the monopile's submerged length (Liaw and Chopra 1974; Goyal and Chopra 1989; Wang P et al. 2018), while SSI is modelled using viscoelastic springs along the embedded length of the monopile (Novak et al. 1978; Das R, Banerjee et al. 2023; Das R, Manna et al. 2023). Further, this study conducts a dynamic analysis of the MSWT in the frequency domain when subjected to the combined action of wind, wave, and ship impact loading, considering variables such as the ship's mass, impact velocity, and point of impact. Additionally, a sensitivity analysis using the Pearson correlation coefficient is performed to examine the sensitivity of the entire system's natural frequency to variations in the geometric and material parameters of the tower, monopile, and soil. Based on the sensitivity analysis,

a simplified non-dimensional model is also proposed, considering non-uniform geometry and representing the foundation with lateral and rotational springs. Furthermore, closed-form expressions for these springs have been derived as a function of the monopile and soil's physical properties. Finally, an analytical approximation for a closed-form expression of the natural frequency has been developed. The closed-form expression of the natural frequency is validated both numerically and experimentally. A flow chart highlighting the complete outline of the present study is provided in Figure 3. This study can assist in the preliminary design of beam-like structures, considering their conicity and flexible supports.

2. Problem statement

The current study is categorised into two main areas: (i) investigating the dynamic response of the MSWT under ship impact loading, depicted in Figure 4(a), and (ii) estimating the natural frequencies of the MSWT. A comprehensive analytical framework is

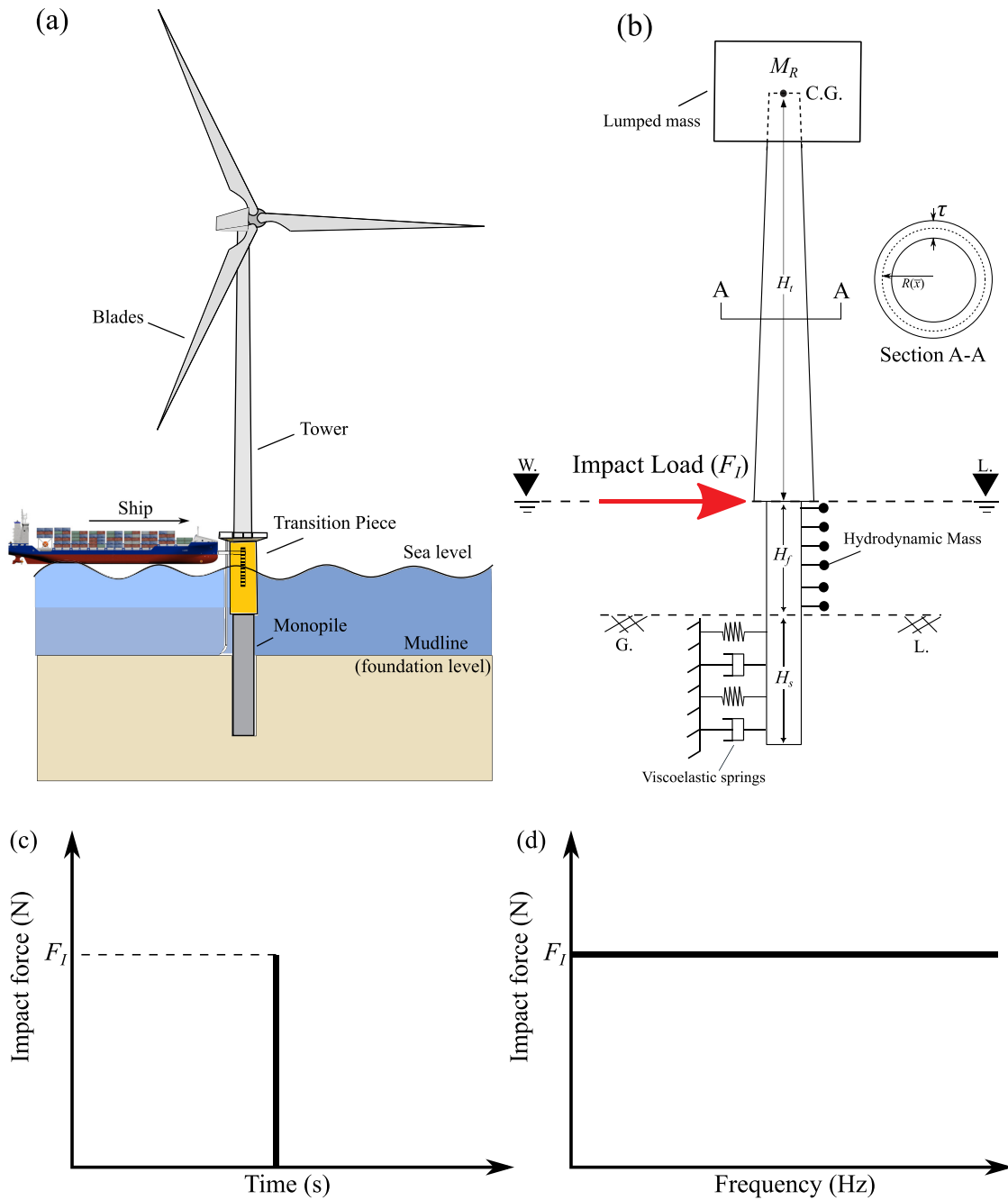


Figure 4. The monopile-supported offshore wind turbine (MSWT) subjected to ship impact used in the present study: (a) Schematic model; (b) Mathematical model; (c) Time domain plot of the impact load; and (d) Corresponding frequency domain plot of the impact load. (This figure is available in colour online.)

adopted to model the MSWT, with detailed mathematical formulations provided for both the superstructure and substructure in Subsections 3.1 and 3.2, respectively. The impact of ship loading is represented by the scenario shown in Figure 4(b), where an Impact force (F_I) is applied at the top of the transition piece. The time and frequency domain plots for this impact load are depicted in Figure 4(c,d), respectively. The study evaluates the dynamic response at the tower's top resulting from the ship's impact loading.

Determining the displacement at the top of a wind turbine tower is crucial for ensuring structural integrity, dynamic stability, and operational efficiency. All the dynamic complications occur at the top of the tower due to the RNA and blades at the top. Thus, when OWT is subjected to any dynamic loads, the displacement will be maximum at the top, and accurate displacement analysis optimises material use, reduces costs, and ensures the tower meets safety and performance criteria while maintaining aerodynamic efficiency

and longevity. A parametric analysis is also conducted to observe how variations in the ship's physical properties affect the maximum dynamic response at the MSWT's top, detailed in Subsection 4.1. Also, the dynamic response due to the combined action of wind and wave load has been detailed in Subsection 4.2. Additionally, a sensitivity analysis is performed in Section 5 to examine how changes in geometric and material properties of the MSWT impact its natural frequencies. Based on the insights gained from the sensitivity analysis, a simplified non-dimensional model is proposed to derive governing dimensionless parameters. Furthermore, an approximate analytical expression for natural frequency is derived in Section 6 by converting the simplified non-dimensional model into a Single Degree of Freedom (SDOF) system.

3. Mathematical formulation

An offshore wind turbine typically comprises three distinct elements: the tower, the submerged section of the monopile, and the portion embedded within the soil, as illustrated in Figure 4(a). Each component is subject to different governing equations that reflect the varied mechanical properties encountered in each environment. Specifically, the tower and monopile are modelled as Euler–Bernoulli beams (Patro, Panda et al. 2024) due to their high slenderness ratio. The rotor nacelle assembly (RNA) and blades are represented as a lumped mass positioned at the tower's top (Arany et al. 2016). Incorporating fluid-structure interaction (FSI) and soil-structure interaction (SSI) is crucial for accurately modelling the submerged monopile section and the subsoil portion. FSI involves the application of rigid hydrodynamic masses on the submerged region's surface to simulate the interaction between the structure and the surrounding water (Wang P et al. 2018). Soil behaviour is modelled using a combination of a spring and a dashpot to mimic its viscoelastic properties. This facilitates the analysis of dynamic interactions between the structure and the soil (Das R, Manna et al. 2023). Consequently, the dynamics of the substructure can be conceptualised as akin to a beam vibrating on a viscoelastic foundation, with the addition of a hydrodynamic mass to represent submerged FSI adequately. Figure 4(b) outlines the mathematical model used for the MSWT in this study. For clarity and focus, the following assumptions have been made in the analysis:

- The tower and monopile are assumed to possess uniform material properties throughout their length and

cross-sections. Euler–Bernoulli beam theory is applied to model both structures to simplify the analysis. While some studies have considered the application of Timoshenko beam theory for modelling the tower, this approach increases the system's complexity without significantly improving the accuracy of natural frequency predictions (Arany, Bhattacharya, Adhikari et al. 2015; Bhattacharya 2019; Bozyigit et al. 2023).

- This investigation emphasises estimating the undamped natural frequency, presenting a more conservative scenario, and helping to prevent resonance (Adhikari and Bhattacharya 2012). Given the primary objective of determining the undamped natural frequency of the complete system and the dynamic response to impact loading, it is presumed that deformations remain small, allowing for the application of linear theory (Damgaard and Andersen 2012).
- The RNA and blades are treated as a lumped mass at the top of the tower, primarily to enhance computational efficiency, especially in managing complex fluid-structure interaction challenges. Similarly, the transition piece that connects the tower and monopile is simulated as an Euler–Bernoulli beam, with geometric and material characteristics assumed to be identical to those of the monopile for simplicity and ease of analysis (Darvishi Alamouti et al. 2020).

3.1. Analytical model of superstructure

This section presents a comprehensive analytical approach to model the tower and the RNA, deriving the dynamic stiffness matrix (DSM) to establish the force-displacement relationship. The Spectral Element Method (SEM) is employed herein to compute the DSM. Unlike the Finite Element Method (FEM), SEM uses a direct Fourier transform (DFT) to convert the tower and pile's governing equation from the time domain to the frequency domain, rendering it a preferable choice for this analysis (Adhikari and Bhattacharya 2021). The mathematical representation of the wind turbine tower consists of a hollow tapered Euler–Bernoulli beam with a length denoted as H_t , depicted in Figure 4(b) (Deng et al. 2023). Consequently, the governing equations governing the tower's transverse motion during free vibration are expressed as per Rao (2019):

$$\frac{\partial^2}{\partial x^2} \left\{ E_t I_t(x) \frac{\partial^2 w_t(x, t)}{\partial x^2} \right\} + \rho_t A_t(x) \frac{\partial^2 w_t(x, t)}{\partial t^2} = 0 \quad (1)$$

In these equations, $w_t(x, t)$ represent the transverse displacements of the tower, respectively, both

dependent on the spatial coordinate x and time t . $E_t I_t(x)$ and $\rho_t A_t(x)$ denote the flexural rigidity and mass per unit length of the tower, respectively. In the case of a tapered section, the radius varies linearly as shown in Figure 4(b), leading to expressions for the area and second moment of area as a function of distance x as follows:

$$\begin{aligned} R(x) &= r_t + (r_b - r_t) \frac{x}{H_t} = r_t(1 + cx); \\ A_t(x) &= 2\pi R(x)\tau = 2\pi r_t(1 + cx)\tau; \\ I_t(x) &= \pi R^3(x)\tau = \pi r_t^3(1 + cx)^3\tau \end{aligned} \quad (2)$$

where $c = \frac{(r_b - r_t)}{H_t}$ is a constant used to account for cross-sectional variation, also referred to as conicity (Boiangiu et al. 2016). $r_b = \frac{D_{tb} - \tau}{2}$ and $r_t = \frac{D_{tt} - \tau}{2}$ are the tower's outside bottom and top radii. Similarly, D_{tb} and D_{tt} are the tower's outside bottom and top diameter. Additionally, τ and H_t represent the thickness and height of the tower section. For solving Equation (1), a harmonic solution can be assumed, represented as $w_t(x, t) = W_t(x)e^{-i\omega t}$, following the approach outlined in (Kreyszig et al. 2008). Here, ω denotes the excitation frequency, and i signifies the imaginary unit. By substituting Equation (2) and the harmonic solutions into Equation (1), we obtain:

$$\begin{aligned} \frac{\partial^2}{\partial x^2} \left((1 + cx)^3 \frac{\partial^2 W_t(x)}{\partial x^2} \right) - \frac{2\omega^2 \rho_t}{E_t r_t^2} (1 + cx) W_t(x) \\ = 0 \end{aligned} \quad (3)$$

By employing Bessel functions (Bowman 2012), solutions for Equation (3) can be derived using mathematical software Maple (Gander and Hrebicek 2004). The expressions are outlined as follows:

$$\begin{aligned} W_t(x) &= \sqrt{\frac{c}{(1 + cx)}} \\ \{I_1(\varepsilon)A_1 + J_1(\varepsilon)A_2 + K_1(\varepsilon)A_3 + Y_1(\varepsilon)A_4\} \\ &= \sum_{j=1}^4 \phi_j(x)A_j \end{aligned} \quad (4)$$

where A_j are the arbitrary constants corresponding to the tower's transverse and axial equations of motion as given in Equation (3). The terms $I_n(\varepsilon)$ and $K_n(\varepsilon)$ denote the n th order modified Bessel functions of the first and second kinds, respectively, while $J_n(\varepsilon)$ and $Y_n(\varepsilon)$ represent the n th order Bessel functions of the first and second kinds, respectively. Moreover, $\varepsilon = \frac{2}{c} \left(\frac{2\rho_t}{E_t r_t^2} \right)^{\frac{1}{4}} \sqrt{\omega(1 + cx)}$. The state vectors, namely rotation (θ_t), bending moment (M_t) and shear force (V_t) associated with a single end of the tower as depicted in Figure 5(b), can be expressed as functions of

transverse displacement as follows:

$$\begin{aligned} \theta_t(x, t) &= W_t^I(x)e^{-i\omega t}, \\ M_t(x, t) &= E_t I_t(x) W_t^{II}(x)e^{-i\omega t}, \\ V_t(x, t) &= \frac{\partial M_t(x, t)}{\partial x} = E_t I_t^I(x) W_t^{II}(x)e^{-i\omega t} \\ &\quad + E_t I_t(x) W_t^{III}(x)e^{-i\omega t} \end{aligned} \quad (5)$$

In this context, $(\bullet)^I$ represents the partial differentiation with respect to spatial coordinates. By substituting Equations (4) into (5), the spectral nodal displacement and slope can be connected to the displacement field as follows:

$$\underbrace{\begin{Bmatrix} w_t(x, t)|_{x=0} \\ \theta_t(x, t)|_{x=0} \\ w_t(x, t)|_{x=H_t} \\ \theta_t(x, t)|_{x=H_t} \end{Bmatrix}}_D = \underbrace{\begin{bmatrix} \phi_1(x)|_{x=0} & \phi_2(x)|_{x=0} & \phi_3(x)|_{x=0} & \phi_4(x)|_{x=0} \\ \phi_1^I(x)|_{x=0} & \phi_2^I(x)|_{x=0} & \phi_3^I(x)|_{x=0} & \phi_4^I(x)|_{x=0} \\ \phi_1(x)|_{x=H_t} & \phi_2(x)|_{x=H_t} & \phi_3(x)|_{x=H_t} & \phi_4(x)|_{x=H_t} \\ \phi_1^I(x)|_{x=H_t} & \phi_2^I(x)|_{x=H_t} & \phi_3^I(x)|_{x=H_t} & \phi_4^I(x)|_{x=H_t} \end{bmatrix}}_H \underbrace{\begin{bmatrix} A_1 \\ A_2 \\ A_3 \\ A_4 \end{bmatrix}}_\Theta e^{-i\omega t} \quad (6)$$

Similarly, substituting Equations (4) in (5), the force state vectors for the tower element shown in Figure 4(b) can be defined as follows:

$$\underbrace{\begin{Bmatrix} V_t(x, t)|_{x=0} \\ M_t(x, t)|_{x=0} \\ V_t(x, t)|_{x=H_t} \\ M_t(x, t)|_{x=H_t} \end{Bmatrix}}_F = \underbrace{\begin{bmatrix} E_t I_t(x)|_{x=0} & E_t I_t^I(x)|_{x=0} & 00 \\ 0 & -E_t I_t(x)|_{x=0} & 00 \\ 0 & 0 - E_t I_t(x)|_{x=H_t} & -E_t I_t^I(x)|_{x=H_t} \\ 0 & 00 & E_t I_t(x)|_{x=H_t} \end{bmatrix}}_X \underbrace{\begin{bmatrix} \phi_1^{III}(x)|_{x=0} & \phi_2^{III}(x)|_{x=0} & \phi_3^{III}(x)|_{x=0} & \phi_4^{III}(x)|_{x=0} \\ \phi_1^{II}(x)|_{x=0} & \phi_2^{II}(x)|_{x=0} & \phi_3^{II}(x)|_{x=0} & \phi_4^{II}(x)|_{x=0} \\ \phi_1^{III}(x)|_{x=H_t} & \phi_2^{III}(x)|_{x=H_t} & \phi_3^{III}(x)|_{x=H_t} & \phi_4^{III}(x)|_{x=H_t} \\ \phi_1^{II}(x)|_{x=H_t} & \phi_2^{II}(x)|_{x=H_t} & \phi_3^{II}(x)|_{x=H_t} & \phi_4^{II}(x)|_{x=H_t} \end{bmatrix}}_G \underbrace{\begin{bmatrix} A_1 \\ A_2 \\ A_3 \\ A_4 \end{bmatrix}}_\Theta e^{-i\omega t} \quad (7)$$

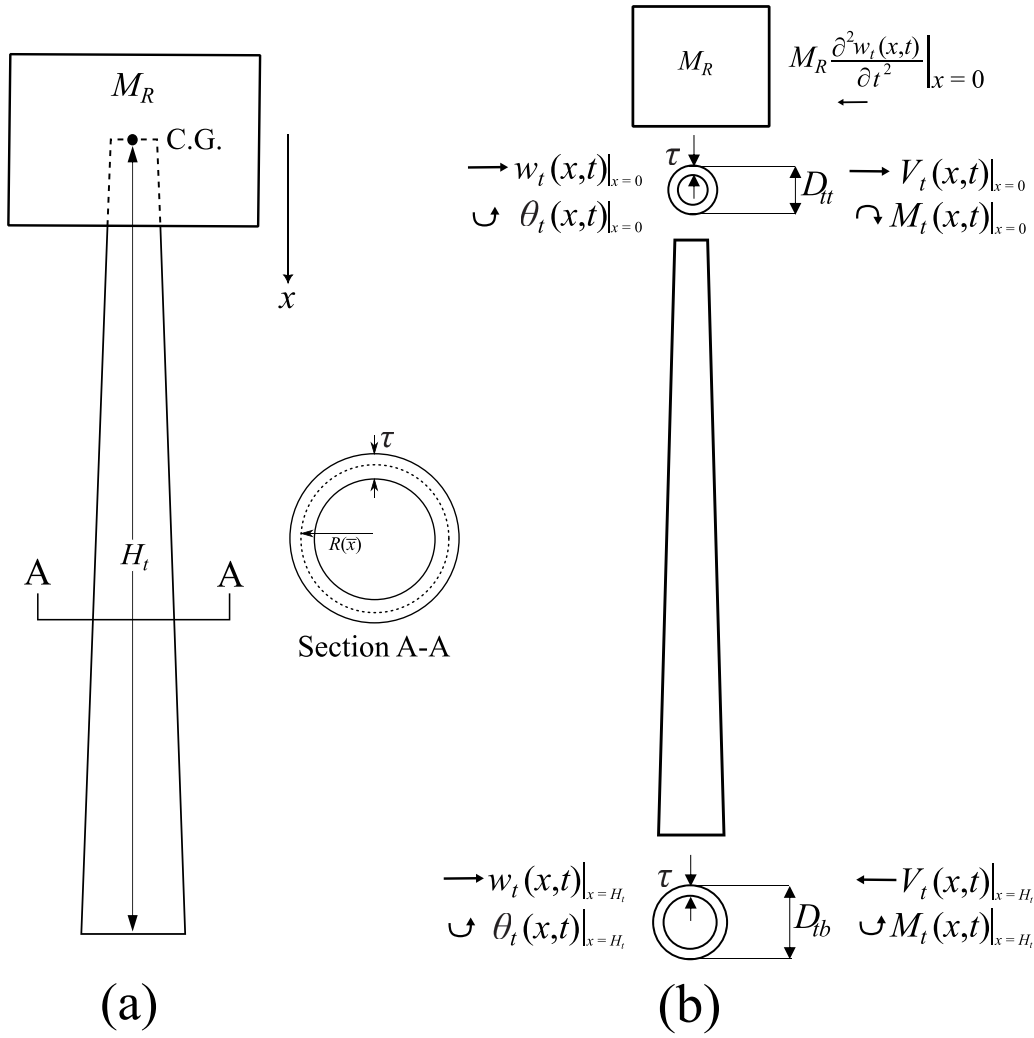


Figure 5. (a) Schematic model of the tower having eccentrically attached rigid body of RNA; (b) Schematic depicting the free body diagram of the tower and (c) Illustration displaying the free body diagram of the rigid body representing the RNA. (This figure is available in colour online.)

Substituting Equations (6) in (7), the force-displacement relationship between the two ends of the tower element can be defined as follows:

$$\mathbf{F} = \mathbf{XG}\mathbf{\Theta} = \mathbf{XGH}^{-1}\mathbf{D} = \mathbf{SD} \quad (8)$$

In this context, $[\mathbf{S}]_{4 \times 4}$ represents the dynamic stiffness matrix (DSM), also referred to as the Spectral Element Matrix (SEM) of the tower. This matrix facilitates establishing a relationship between the forces and displacements at the two ends of the tower (Lee 2009). The subsequent section elaborates on deriving the DSM of the substructure, considering the monopile, soil, and fluid components.

3.2. Analytical model of substructure

This subsection presents a comprehensive analytical approach to model the monopile, considering the

interactions between fluid and SSI. Additionally, it establishes the DSM of the monopile by defining the force-displacement relationship between its two ends. The mathematical representation of the monopile comprises a hollow Euler-Bernoulli beam with a length denoted as $H_f + H_s$, maintaining uniform geometry throughout its height, as depicted in Figure 6(a). Consequently, the governing equations governing the monopile's transverse motion when submerged in water are provided by Liaw and Chopra (1974):

$$E_p I_p \frac{\partial^4 w_f(x_f, t)}{\partial x_f^4} + \left\{ \rho_p A_p + m(x_f) \right\} \frac{\partial^2 w_f(x_f, t)}{\partial t^2} = 0 \quad (9)$$

Here, $E_p I_p(x_f)$ and $\rho_p A_p(x_f)$ denote the flexural rigidity and mass per unit length of the monopile, respectively. $w_f(x_f, t)$ represents the transverse displacement of the monopile submerged in water. The term $m(x_f)$ signifies

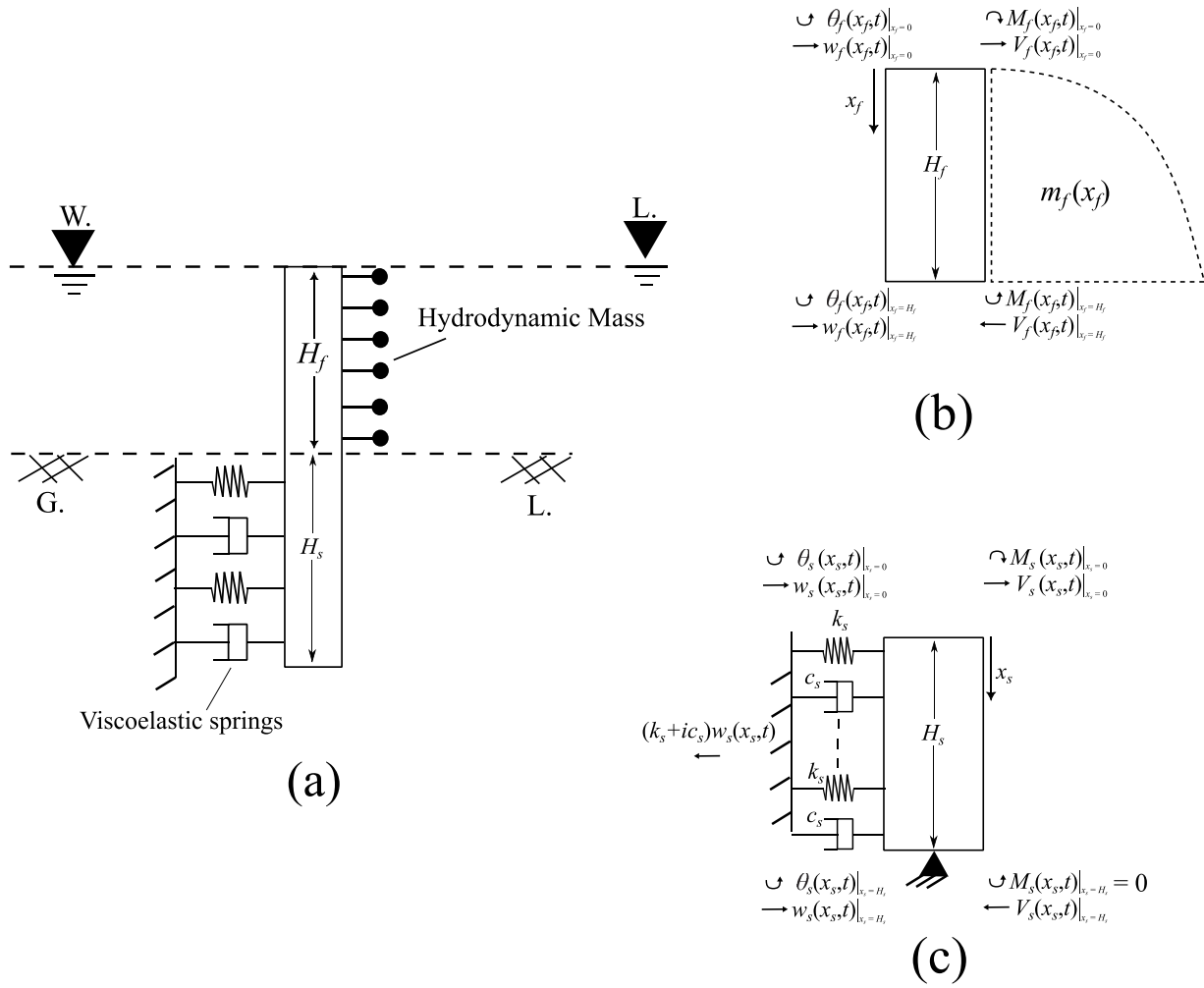


Figure 6. (a) Schematic diagram illustrating the monopile model, accounting for both soil-structure interaction and fluid-structure interaction effects; (b) Illustration showing the free body diagram of the monopile incorporating hydrodynamic mass; (c) Schematic depicting the free body diagram of the monopile equipped with viscoelastic springs. (This figure is available in colour online.)

the hydrodynamic mass, which characterises the lateral resistance at the water-pile interface (Goyal and Chopra 1989). This mass is dependent on the coordinate axis (x_f) and is expressed using Bessel functions, with its calculation defined by the following equation (Wang P et al. 2018):

$$m(x_f) = \frac{16\rho_w H_f r_p}{\pi} \sum_{j=1}^{\infty} \frac{(-1)^{j-1}}{(2j-1)^2} \frac{K_1(\Gamma r_p)}{K_0(\Gamma r_p) + K_2(\Gamma r_p)} \cos(\Gamma x_f) \quad (10)$$

Here, H_f represents the depth of the monopile submerged in water, ρ_w denotes the density of water, r_p signifies the outside radius of the monopile, and $\Gamma = \frac{(2j-1)\pi}{2H_f}$. Utilizing the harmonic solution, namely $w_f(x_f, t) = W_f(x_f)e^{-i\omega t}$, and substituting it into

Equation (9), we obtain:

$$E_p I_p \frac{\partial^4 W_f(x_f)}{\partial x_f^4} - \omega^2 \left\{ \rho_p A_p + m(x_f) \right\} W_f(x_f) = 0 \quad (11)$$

Assuming a uniform section, where both $E_p I_p$ and $\rho_p A_p$ remain constant throughout the beam's entire length, the solution to the transverse equation can be formulated using hyperbolic trigonometric functions (Kreyszig 2013) as follows:

$$W_f(x_f) = C_1 \sin(\alpha x_f) + C_2 \cos(\alpha x_f) + C_3 \sinh(\alpha x_f) + C_4 \cosh(\alpha x_f) \quad (12)$$

where C_1 through C_4 represent unknown arbitrary constants for the transverse equation of motion of the monopile submerged in water. α represents the wave numbers for the monopile element submerged in

water. By substituting Equations (12) in (11), the wave number α can be expressed as a function of the excitation frequency ω as follows:

$$E_p I_p \alpha^4 W_f(x_f) - \omega^2 \{ \rho_p A_p + m(x_f) \} W_f(x_f) = 0$$

$$\Rightarrow \alpha = \sqrt[4]{4} \frac{\omega^2 \{ \rho_p A_p + m(x_f) \}}{E_p I_p} \quad (13)$$

Similar to Equation (5), the state vectors associated with one end of the monopile element submerged in water, as depicted in Figure 6(b), can be expressed in terms of transverse displacement $w_f(x_f, t)$ as follows:

$$\theta_f(x_f, t) = W_f^I(x_f) e^{-i\omega t}, M_f(x_f, t) = E_p I_p(x_f) W_f^{II}(x_f) e^{-i\omega t},$$

$$V_f(x_f, t) = E_p I_p(x_f) W_f^{III}(x_f) e^{-i\omega t} \quad (14)$$

Substituting Equations (12) in (14), the displacement and force state vectors can be written in matrix form as follows:

$$\underbrace{\begin{Bmatrix} w_f(x_f, t)|_{x_f=0} \\ \theta_f(x_f, t)|_{x_f=0} \\ w_f(x_f, t)|_{x=H_f} \\ \theta_f(x_f, t)|_{x=H_f} \end{Bmatrix}}_{\mathbf{D}_f} = \underbrace{\begin{bmatrix} 0 & 1 & 0 & 1 \\ \alpha & 0 & \alpha & 0 \\ \sin(\alpha H_f) & \cos(\alpha H_f) & \sinh(\alpha H_f) & \cosh(\alpha H_f) \\ \alpha \cos(\alpha H_f) & -\alpha \sin(\alpha H_f) & \alpha \cosh(\alpha H_f) & \alpha \sinh(\alpha H_f) \end{bmatrix}}_{\mathbf{K}_f} \underbrace{\begin{bmatrix} C_1 \\ C_2 \\ C_3 \\ C_4 \end{bmatrix}}_{\mathbf{\Theta}_f} e^{-i\omega t} \quad (15)$$

and,

$$\underbrace{\begin{Bmatrix} V_f(x_f, t)|_{x_f=0} \\ M_f(x_f, t)|_{x_f=0} \\ V_f(x_f, t)|_{x_f=H_f} \\ M_f(x_f, t)|_{x_f=H_f} \end{Bmatrix}}_{\mathbf{F}_f} = \underbrace{\begin{bmatrix} E_p I_p & 0 & 0 \\ 0 & -E_p I_p & 0 \\ 0 & 0 & -E_p I_p \\ 0 & 0 & E_p I_p \end{bmatrix}}_{\mathbf{X}_p} \times \underbrace{\begin{bmatrix} -\alpha^3 & 0\alpha^3 & 0 \\ 0 & -\alpha^2 & 0\alpha^2 \\ -\alpha^3 \cos(\alpha H_f) & \alpha^3 \sin(\alpha H_f) & \alpha^3 \cosh(\alpha H_f) & \alpha^3 \sinh(\alpha H_f) \\ -\alpha^2 \sin(\alpha H_f) & -\alpha^2 \cos(\alpha H_f) & \alpha^2 \sinh(\alpha H_f) & \alpha^2 \cosh(\alpha H_f) \end{bmatrix}}_{\mathbf{G}_f} \underbrace{\begin{bmatrix} C_1 \\ C_2 \\ C_3 \\ C_4 \end{bmatrix}}_{\mathbf{\Theta}_f} e^{-i\omega t} \quad (16)$$

Now, using Equations (15) and (16), the force-displacement relationship between the two ends of the monopile element submerged in water can be defined as:

$$\mathbf{F}_f = \mathbf{X}_p \mathbf{G}_f \mathbf{\Theta}_f = \mathbf{X}_p \mathbf{G}_f \mathbf{K}_f^{-1} \mathbf{D}_f = \mathbf{S}_f \mathbf{D}_f \quad (17)$$

Here, $[\mathbf{S}_f]_{4 \times 4}$ is the DSM for the monopile element submerged in water, which is expressed as follows:

$$\mathbf{S}_f = \begin{bmatrix} S_{f11} & S_{f12} & S_{f13} & S_{f14} \\ S_{f12} & S_{f22} & -S_{f22} & S_{f24} \\ S_{f13} & -S_{f14} & S_{f11} & -S_{f12} \\ S_{f14} & S_{f24} & -S_{f12} & S_{f22} \end{bmatrix} \quad (18)$$

where,

$$S_{f11} = -\frac{E_p I_p \alpha^3 (\cosh(\alpha H_f) \sin(\alpha H_f) + \cos(\alpha H_f) \sinh(\alpha H_f))}{\cos(\alpha H_f) \cosh(\alpha H_f) - 1}$$

$$S_{f12} = -\frac{E_p I_p \alpha^2 \sin(\alpha H_f) \sinh(\alpha H_f)}{\cos(\alpha H_f) \cosh(\alpha H_f) - 1}$$

$$S_{f13} = \frac{E_p I_p \alpha^3 (\sin(\alpha H_f) + \sinh(\alpha H_f))}{\cos(\alpha H_f) \cosh(\alpha H_f) - 1}$$

$$S_{f14} = \frac{E_p I_p \alpha^2 (\cos(\alpha H_f) - \cosh(\alpha H_f))}{\cos(\alpha H_f) \cosh(\alpha H_f) - 1}$$

$$S_{f22} = \frac{E_p I_p \alpha (\cos(\alpha H_f) \sinh(\alpha H_f) - \cosh(\alpha H_f) \sin(\alpha H_f))}{\cos(\alpha H_f) \cosh(\alpha H_f) - 1}$$

$$S_{f24} = \frac{E_p I_p \alpha^2 (\cos(\alpha H_f) - \cosh(\alpha H_f))}{\cos(\alpha H_f) \cosh(\alpha H_f) - 1} \quad (19)$$

Now, to model the monopile embedded in the soil, the governing differential equation for the transverse motion can be defined as follows (Das R, Banerjee et al. 2023):

$$E_p I_p \frac{\partial^4 w_s(x_s, t)}{\partial x_s^4} + \rho_p A_p \frac{\partial^2 w_s(x_s, t)}{\partial t^2} + (k_s + i c_s) w_s(x_s, t) = 0 \quad (20)$$

Here, $w_s(x_s, t)$ represents the transverse displacement of the monopile embedded in the soil. The parameters k_s and c_s denote the viscoelastic properties of the spring-dashpot system in terms of stiffness and dashpot coefficients, specifically $k_s = G_s S_{u1}$ and $c_s = G_s S_{u2}$. Here, G_s stands for the shear modulus of the soil medium. At the same time, S_{u1} and S_{u2} represent solutions to the viscoelastic equation of motion of the soil, expressed in cylindrical coordinate system terms. These parameters primarily function the excitation frequency ω and Poisson's ratio μ_s . Further details regarding S_{u1} and S_{u2} can be found in (Novak 1974). Similar to previous instances, a harmonic solution to Equation (20) can be assumed as $w_s(x_s, t) = W_s(x_s) e^{-i\omega t}$ and substituted

into Equation (20) to obtain:

$$E_p I_p \frac{\partial^4 W_s(x_s)}{\partial x_s^4} + (k_s + ic_s - \omega^2 \rho_p A_p) W_s(x_s) = 0 \quad (21)$$

Similar to Equation (12) trigonometric hyperbolic solutions can be obtained to Equation (21) as follows:

$$W_s(x_s) = D_1 \sin(\beta x_s) + D_2 \cos(\beta x_s) + D_3 \sinh(\beta x_s) + D_4 \cosh(\beta x_s) \quad (22)$$

where D_1 through D_4 represent unknown arbitrary constants for the transverse equation of motion of the monopile embedded in the soil. β represents the wave numbers for the monopile element embedded in the soil. By substituting Equations (12) in (11), the wave number β can be expressed as a function of the excitation frequency ω as follows:

$$E_p I_p \beta^4 W_s(x_s) + (k_s + ic_s - \omega^2 \rho_p A_p) W_s(x_s) = 0$$

$$\Rightarrow \beta = \sqrt[4]{\frac{\omega^2 \rho_p A_p - (k_s + ic_s)}{E_p I_p}} \quad (23)$$

Similarly, employing Equations (14)–(19), the DSM for the monopile element embedded in the soil can be derived. To thoroughly investigate the dynamic behaviour of the entire monopile, the DSM of the monopile embedded in soil and submerged in water is combined into a unified global matrix. The process of globalising the force vectors, displacement vectors, and DSM is established using the finite element concept (Cook 2007) and can be expressed as follows:

$$\begin{Bmatrix} V_f(x_f, t)|_{x_f=0} \\ M_f(x_f, t)|_{x_f=0} \\ V_f(x_f, t)|_{x_f=H_f} + V_s(x_s, t)|_{x_s=0} \\ M_f(x_f, t)|_{x_f=H_f} + M_s(x_s, t)|_{x_s=0} \\ V_s(x_s, t)|_{x_s=H_s} \\ M_s(x_s, t)|_{x_s=H_s} \end{Bmatrix} = \begin{Bmatrix} S_{f11} & S_{f12} & S_{f13} & S_{f14} & 0 & 0 \\ S_{f12} & S_{f22} & -S_{f14} & S_{f24} & 0 & 0 \\ S_{f13} & -S_{f14} & S_{f11} + S_{s11} & -S_{f12} + S_{s12} & S_{s13} & S_{s14} \\ S_{f11} & S_{f24} & -S_{f12} + S_{s12} & S_{f22} + S_{s22} & -S_{s14} & S_{s24} \\ 0 & 0 & S_{s13} & -S_{s14} & S_{s11} & -S_{s12} \\ 0 & 0 & S_{s14} & S_{s24} & -S_{s12} & S_{s22} \end{Bmatrix} \times \begin{Bmatrix} w_f(x_f, t)|_{x_f=0} \\ \theta_f(x_f, t)|_{x_f=0} \\ w_f(x_f, t)|_{x_f=H_f} + w_s(x_s, t)|_{x_s=0} \\ \theta_f(x_f, t)|_{x_f=H_f} + \theta_s(x_s, t)|_{x_s=0} \\ w_s(x_s, t)|_{x_s=H_s} \\ \theta_s(x_s, t)|_{x_s=H_s} \end{Bmatrix} \quad (24)$$

The subsequent section of this chapter presents the derivation of the global DSM, which combines the contributions from the tower, RNA, and monopile. Additionally, it outlines a methodology to incorporate the boundary conditions and to evaluate the dynamic response of the MSWT due to the impact loading.

3.3. Boundary conditions and impact loading

This section provides a comprehensive analytical methodology to obtain the dynamic response of the MSWT subjected to impact loading. Initially, by utilising Equations (24) and (8), the global DSM integrating contributions from the tower and monopile can be derived as follows:

$$\underbrace{\begin{Bmatrix} V_t(x, t)|_{x=0} \\ M_t(x, t)|_{x=0} \\ \vdots \\ V_s(x_s, t)|_{x_s=H_s} \\ M_s(x_s, t)|_{x_s=H_s} \end{Bmatrix}}_{F_G} = \underbrace{\begin{bmatrix} S_{11} & S_{12} & \cdots & 0 & 0 \\ S_{12} & S_{22} & \cdots & 0 & 0 \\ \vdots & \vdots & \ddots & \vdots & \vdots \\ 0 & 0 & \cdots & S_{s11} & -S_{s12} \\ 0 & 0 & \cdots & -S_{s12} & S_{s22} \end{bmatrix}}_{S_G} \underbrace{\begin{Bmatrix} w_t(x, t)|_{x=0} \\ \theta_t(x, t)|_{x=0} \\ \vdots \\ w_s(x_s, t)|_{x_s=H_s} \\ \theta_s(x_s, t)|_{x_s=H_s} \end{Bmatrix}}_{D_G} \quad (25)$$

Here, $[S_G]_{8 \times 8}$ denotes the global dynamic stiffness matrix (DSM) or global Spectral Element Matrix (SEM), which establishes the global frequency dependent force-displacement relationship across the entire MSWT. Due to the lumped mass at the top of the tower, as shown in Figure 5(b), an additional shear force will act, which is defined as follows:

$$V_t(x, t)|_{x=0} = -M_R \omega^2 w_t(x, t)|_{x=0} = -S_{MR} w_t(x, t)|_{x=0} \quad (26)$$

Additionally, due to the impact load at the top of the monopile as shown in Figure 4(b), a forcing term of F_I will be applied in the force matrix, and all other shear forces and bending moments in the forcing matrix will be zero. Thus, the dynamic response of the MSWT can be obtained by modifying Equation (25)

as follows:

$$\underbrace{\begin{Bmatrix} 0 \\ 0 \\ F_I \\ 0 \\ 0 \\ 0 \\ 0 \\ 0 \end{Bmatrix}}_{\mathbf{F}_G} = \underbrace{\begin{bmatrix} S_{11} - S_{MR} & S_{12} & \cdots & 0 & 0 \\ S_{12} & S_{22} & \cdots & 0 & 0 \\ \vdots & \vdots & \ddots & \vdots & \vdots \\ 0 & 0 & \cdots & S_{s11} & -S_{s12} \\ 0 & 0 & \cdots & -S_{s12} & S_{s22} \end{bmatrix}}_{\mathbf{S}_G, 8 \times 8} \quad (27)$$

$$\underbrace{\begin{Bmatrix} w_t(x, t)|_{x=0} \\ \theta_t(x, t)|_{x=0} \\ \vdots \\ w_s(x_s, t)|_{x_s=H_s} \\ \theta_s(x_s, t)|_{x_s=H_s} \end{Bmatrix}}_{\mathbf{D}_G, 8 \times 1} \Rightarrow \mathbf{D}_G = \mathbf{S}_G^{-1} \mathbf{F}_G$$

Here, $\mathbf{D}_G(1, 1)$ represents the dynamic response at the tower top. Since the displacement at the RNA is expected to be at its peak under impact loading, this study will focus on analyzing the maximum displacement observed at the top of the tower. The subsequent section provides the details of wind and wave loads applied to the wind turbine.

3.4. Wind and wave loads

This study represents wind and wave loads by their respective power spectral densities (PSD), as shown

in Figure 7. The Kaimal spectrum (Kaimal et al. 1972) represents the wind load, while the JONSWAP spectrum (Isherwood 1987) represents the wave loads. The spectral density of the turbulent gust drag force, which incorporates spatial correlation information, can be defined following Patro, Panda et al. (2024)

$$S_{\bar{\omega}_x \bar{\omega}_y}(\bar{\omega}, z) = (\rho_a \bar{U}(z))^2 (A_T^2 C_D^2 + C_T^2 A_R^2) S_{u_x u_y}(\bar{\omega}) \chi^2(\bar{\omega}) \quad (28)$$

Here, ρ_a is the air density, $\bar{U}(z)$ is the wind velocity at $z = H_t - x$, A_T denotes the average cross-sectional area of the tower, C_D represents the drag coefficient of the wind turbine tower, C_T is the thrust coefficient, and A_R stands for the cross-sectional area of the rotor. χ represents aerodynamic admittance and $S_{u_x u_y}(\bar{\omega})$ is the cross-power spectral density function of fluctuating wind speed. More details on $S_{u_x u_y}(\bar{\omega})$ can be found in Patro, Panda et al. (2024). Similarly, the expression of the power spectrum of the wave force exerted on the monopile can be defined as follows:

$$S_{FF, waves}(\bar{\omega}, z_w) = C_m^2 \rho_w^2 \frac{D_p^4 \pi^6}{4x_f} \frac{\bar{\omega}^4}{\sinh^2(\psi S)} \left\{ \left(\frac{S}{2\psi} - \frac{1}{2\psi^2} \right) e^{\psi S} - \left(\frac{S}{2\psi} + \frac{1}{2\psi^2} \right) e^{-\psi S} + \frac{1}{\psi^2} \right\}^2 S_{ww}(\bar{\omega}) \quad (29)$$

In this equation, C_m represents the inertia coefficient, ρ_w is the water density, D_p denotes the outer diameter of the monopile, x_f is the vertical coordinate of the submerged monopile in water, S is the mean sea

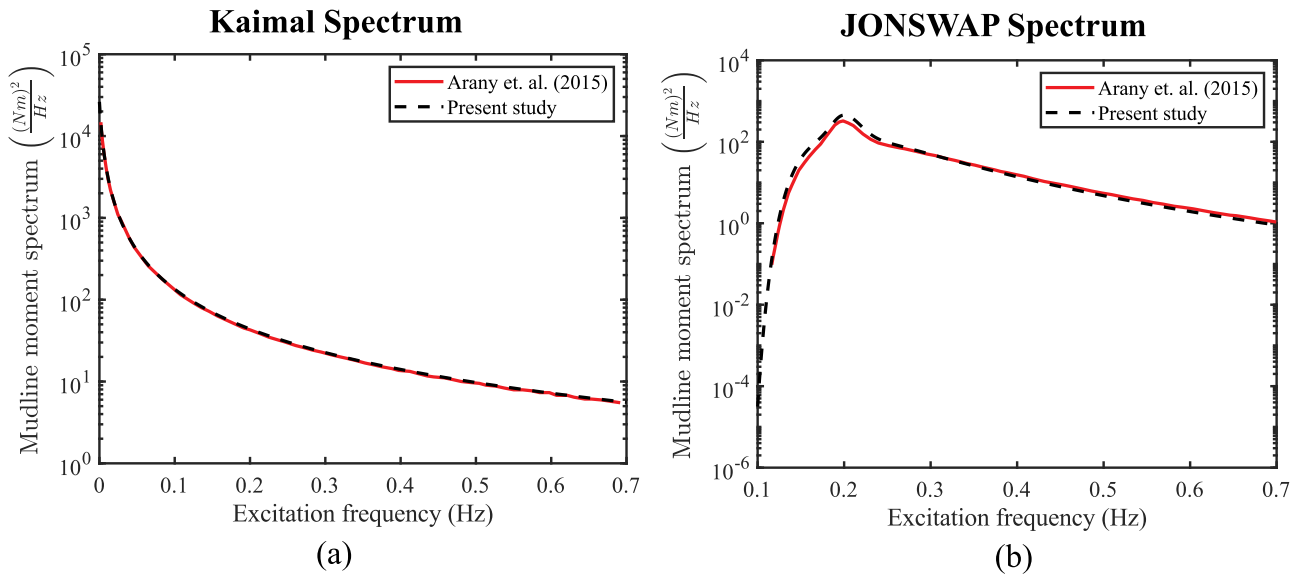


Figure 7. (a) and (b) Variation of forcing spectrum with excitation frequency for wind and wave load. These spectra are shown as mudline moment spectra validated with Arany, Bhattacharya, Macdonald et al. (2015) for (a) Kaimal Spectrum and (b) JONSWAP Spectrum. (This figure is available in colour online.)

depth and ψ signifies the wave number. The term $S_{ww}(\bar{\omega})$ characterises the ocean wave, defined as a zero-mean stationary stochastic process, also referred to as a PSD function. More details on $S_{ww}(\bar{\omega})$ can be found in Patro, Panda et al. (2024). The subsequent section provides the variation of the ship's different physical properties with the dynamic response of the MSWT.

4. Dynamic response analysis

4.1. Ship impact only

In Figure 8(a), the graph illustrates how the displacement response at the RNA varies with the excitation frequency across different Relative mass (R_M) values, defined as the ratio of the ship's mass to the MSWT's mass. The ship's mass is critical in MSWT dynamic analysis, as a higher mass translates to a more significant impact. The Vestas V90 3 MW wind turbine (Romero et al. 2016) model is considered in the present study, and its geometric and material properties are given in Table 1. In this study, the ship's mass ranges from 0.5 to 5 times that of the MSWT. The graph in Figure 8(a) indicates a direct correlation between the

dynamic response of the MSWT and the variation in R_M . Peaks in the displacement response across all R_M values signify the natural frequency of the MSWT. Furthermore, Figure 8(d) displays the variation of peak displacement response for different R_M values. Notably, while the peak displacement response increases with R_M , the rate of increase gradually slows down, eventually reaching a constant.

In Figure 8(b), the graph depicts how the displacement response at the RNA varies with excitation frequency across different Relative height (R_H) values, representing the ratio of the submerged monopile height to its total height. The variation in water depth determines the impact location, with water height ranging from 0.05 to 0.5 times the monopile's total height in this study. Observing Figure 8(b), it's evident that the MSWT's dynamic response is directly proportional to changes in R_H . Additionally, there's a noticeable leftward shift in the peak displacement response at the RNA with increasing R_H values. This shift indicates a decrease in the MSWT's natural frequency as R_H increases. The higher water depth leads to greater hydrodynamic mass, reducing the system's natural frequency. Furthermore, Figure 8(e) illustrates the variation in peak displacement response

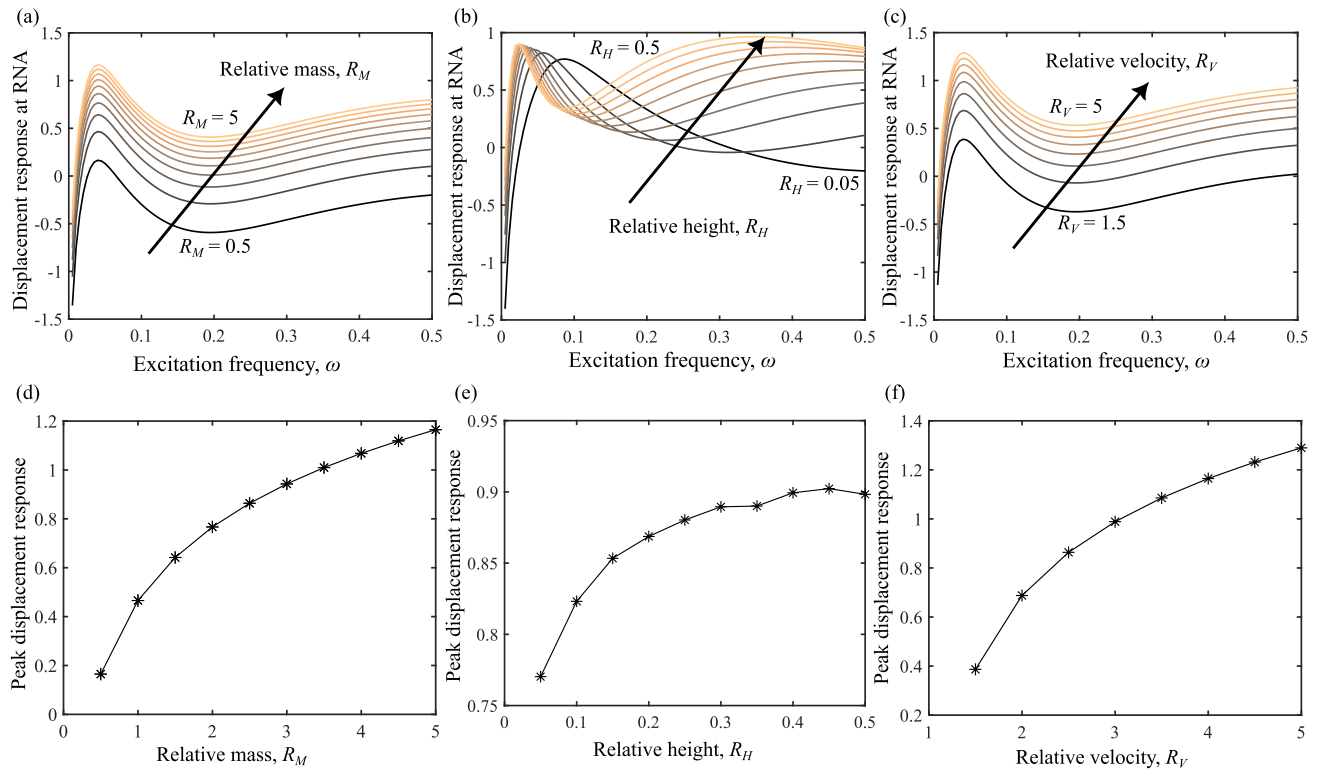


Figure 8. Variation of the ship's different physical properties with the dynamic response of the MSWT: (a)–(c) Displacement response at RNA with excitation frequency for different (a) Relative mass (ratio of the mass of ship to the mass of MSWT); (b) Relative height (ratio of the height of monopile submerged in water to the total height of monopile); (c) Relative velocity (ratio of the impact velocity of the ship to the initial velocity of the ship); (d)–(f) Maximum displacement response with (d) Relative mass; (e) Relative height; and (f) Relative velocity. (This figure is available in colour online.)

Table 1. Physical properties of the Vestas V90 3 MW wind turbine (Romero et al. 2016).

Components	Properties	Values
Tower	Length, H_t (m)	80
	Top outside diameter, D_{tt} (m)	2.31
	Bottom outside diameter, D_{tb} (m)	4.2
	Wall thickness, τ (mm)	30
	Young's modulus, E_t (GPa)	210
	Density, ρ_t (kg/m ³)	7850
	RNA mass, M_R (tonne)	111
Monopile	Length, H_p (m)	28
	Outside diameter, D_p (m)	4.3
	Wall thickness, t_p (mm)	45
	Density, ρ_p (kg/m ³)	7850
	Young's modulus, E_p (GPa)	210
	Mean sea depth, H_f (m)	8
	Young's modulus, E_s (MPa)	20
Soil	Density, ρ_s (kg/m ³)	1500
	Poisson's ratio, μ_s	0.3

for different R_H values. Here, the rate of increase gradually diminishes and stabilises as water depth increases.

Finally, Figure 8(c) shows the variation of displacement response at RNA with excitation frequency for different values of Relative velocity (R_V), which is defined as the ratio of the impact velocity of the ship (v_I) to the initial velocity (v_0) of the ship (Bela et al. 2017). The impact velocity and the mass of the ship (M_S) directly influence the impact force with the help of the following equation:

$$F_I = \frac{M_S \times (v_I - v_0)}{\Delta t} \quad (30)$$

Here, Δt represents the time the impact occurs. Hence, the dynamic response profile for Relative velocity (R_V) is expected to resemble that of Relative mass (R_M), as

illustrated in Figure 8(c). In this study, the initial velocity of the ship (v_0) is set at 1 m/s, while the ship's impact velocity (v_I) is varied from 1.5 to 5 times v_0 . The impact velocity can exceed its initial velocity due to elastic collisions, external forces (e.g. propulsion or waves), or energy transfer from the impacted object (Pedersen et al. 1993). The time duration of impact, denoted as Δt , is kept constant at 0.1 seconds. Similar to the preceding cases, the variations in peak displacement response across different R_V values are depicted in Figure 8(d).

4.2. Combined action of wind and wave loading

In this section, the dynamic response of the MSWT is obtained when subjected to the combined action of ship impact, wind loads, and wave loads, as shown in Figure 9. The dynamic wind and wave forces as a function of excitation frequency are calculated using Equations (28) and (29). In Figure 9(a), a single peak is observed, corresponding to the natural frequency of the entire system. However, in Figure 9(b), an additional peak is observed apart from the resonant frequency, primarily due to the peak frequency of the wave load.

5. Eigenvalues and simplified analytical model of MSWT

From Figure 8, it is observed that the maximum dynamic response occurs at the resonant frequency of the MSWT for all the cases of ship loading. Thus, correctly estimating the natural frequency of the entire

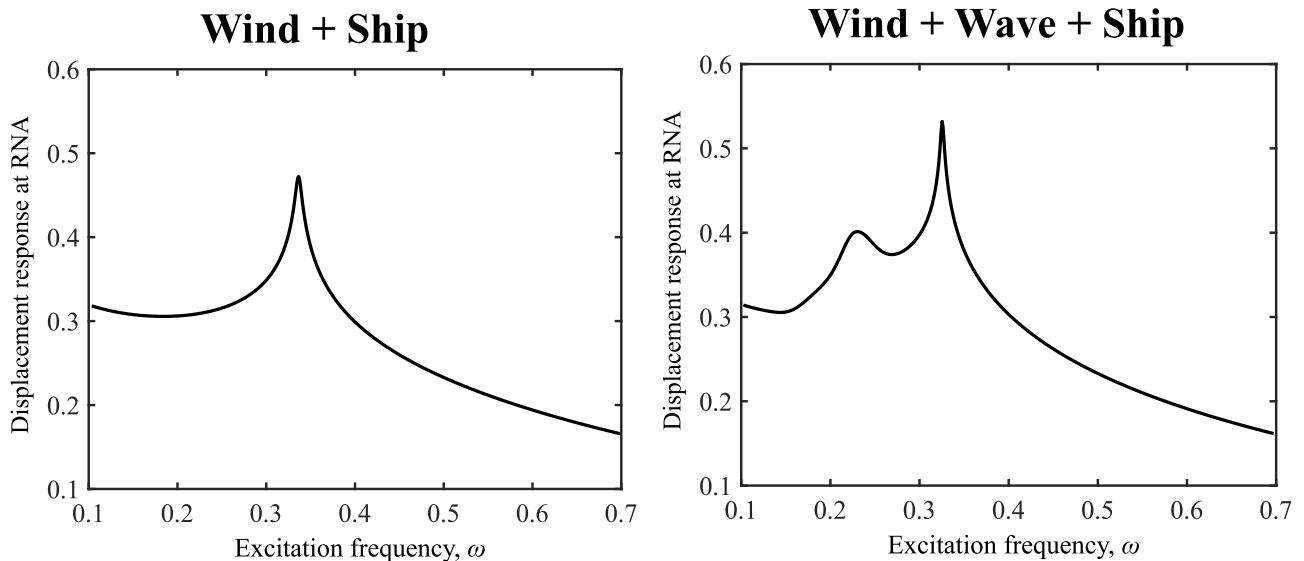


Figure 9. Dynamic response of MSWT is obtained when subjected to the combined action of (a) Wind + Ship impact and (b) Wind + Wave + Ship Impact. (This figure is available in colour online.)

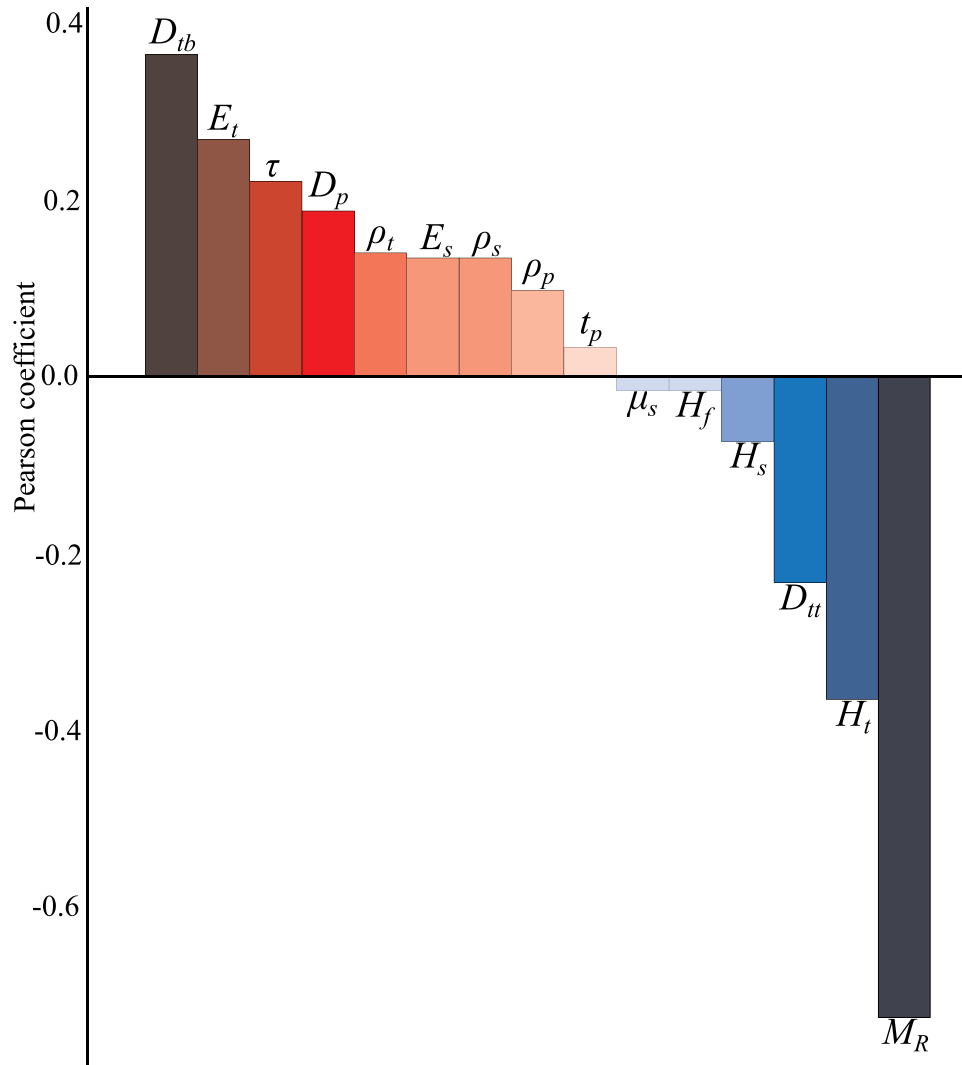


Figure 10. Natural frequency variation with different geometric and material parameters given in Table 3. (This figure is available in colour online.)

system is highly necessary. Subsequently, this section provides the details for calculating the natural frequency of the entire system by conducting the eigenvalue analysis. To conduct the eigenvalue analysis, the determinant of $[\mathbf{S}_G]_{8 \times 8}$ is equated to zero. Since $[\mathbf{S}_G]_{8 \times 8}$ is a function of ω , solving the expression of $[\mathbf{S}_G]$ enables us to identify the system's eigenfrequencies (Das A et al. 2024). The first eigenfrequency corresponds to the natural frequency of the entire system. Moreover, a sensitivity analysis has investigated the natural frequency variation concerning geometric and material parameters outlined in Table 3. The sensitivity analysis uses Pearson correlation, as illustrated in Figure 10. In the Pearson correlation graph presented in Figure 10, parameters exhibiting positive values indicate a direct relationship with the natural frequency and vice versa (Panda et al. 2023). Higher absolute values (positive or negative) of parameters suggest a greater sensitivity towards the

natural frequency and vice versa. From the sensitivity analysis, it's observed that the mass of the RNA (M_R) and the bottom diameter of the tower (D_{tb}) exhibit more sensitivity towards the natural frequency. Hence, emphasising these parameters in the MSWT design process is crucial. However, parameters such as the depth of the monopile submerged in water (H_f) exhibit negligible influence on the natural frequency. Consequently, a simplified model has been proposed in subsequent subsections to reduce the computational complexity and time associated with the current analytical model.

This subsection converts the existing analytical model illustrated in Figure 11(a) into a simplified model depicted in Figure 11(b). In this simplified model, the RNA is represented as a lumped mass positioned at the top of the tower. In contrast, the effects of Fluid-Structure Interaction (FSI) and soil-structure interaction (SSI) are modelled using a two-spring

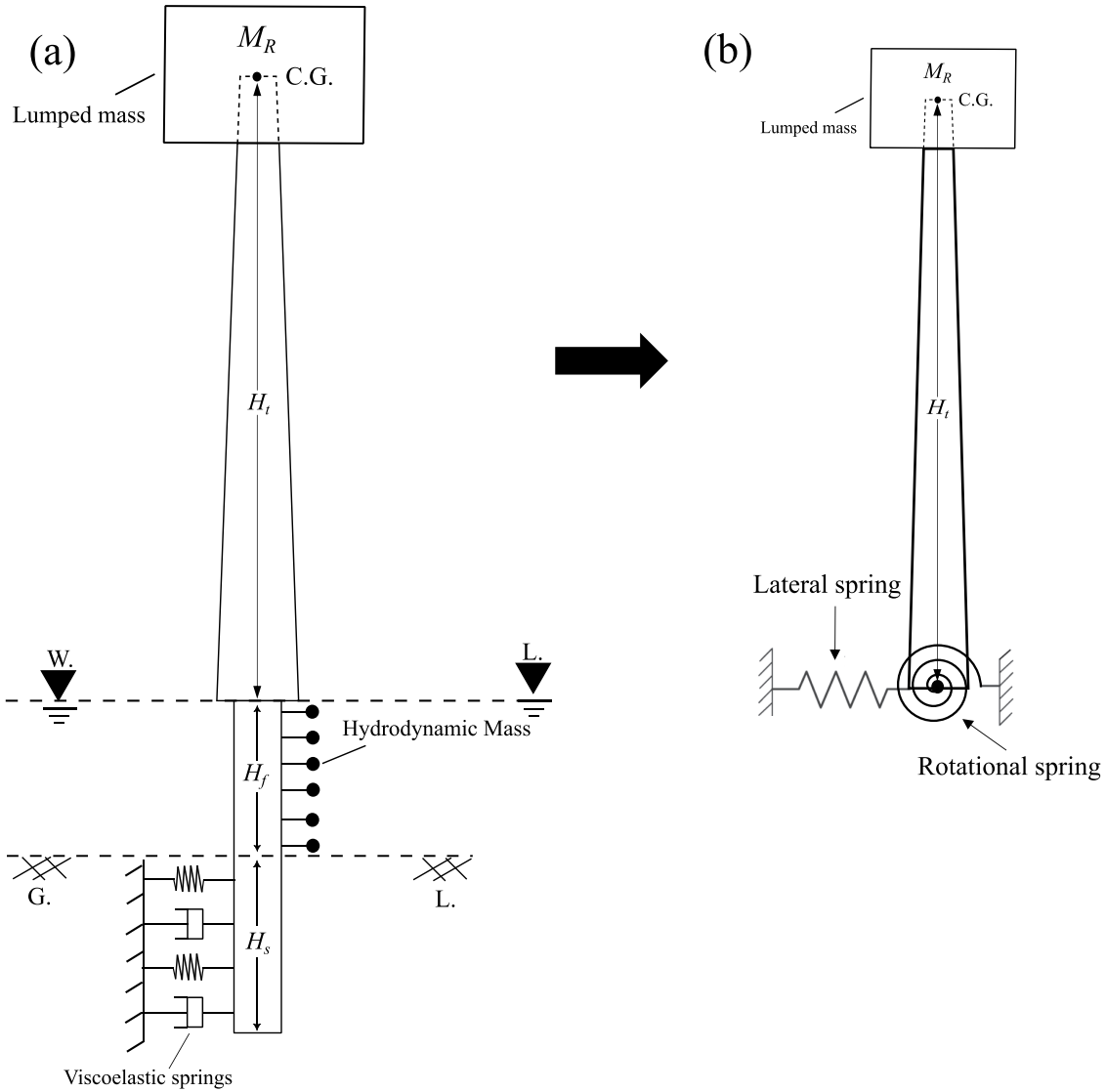


Figure 11. (a) The mathematical model depicting an eccentric rigid body and accounting for the effects of FSSI; (b) A simplified system incorporating a lumped mass and a two-spring substructure system. (This figure is available in colour online.)

substructure approach with lateral and rotational degrees of freedom. Due to the inclusion of a lumped mass at the top in the simplified model, only transverse displacement is considered to model the tower, i.e. according to Equation (1). Now, by introducing non-dimensional parameters for space, time, and transverse displacement, denoted as $\bar{x} = \frac{x}{H_t}$, $\bar{t} = \omega_n t$, and $\bar{w} = \frac{w}{\omega}$, respectively, and substituting them into Equation (1), the non-dimensionalized differential equation for the tower can be formulated as follows:

$$\frac{\partial^2}{\partial \bar{x}^2} \left[(1 + \bar{c}\bar{x})^3 \frac{\partial^2 \bar{w}(\bar{x}, \bar{t})}{\partial \bar{x}^2} \right] + (1 + \bar{c}\bar{x}) \frac{\partial^2 \bar{w}(\bar{x}, \bar{t})}{\partial \bar{t}^2} = 0 \quad (31)$$

where, ω and $\omega_n = \sqrt{\frac{E_t r_t^2}{2\rho_t H_t^4}}$ represent arbitrary constants bearing the units of dimensional quantity, while $\bar{c} = cH_t$ denotes the non-dimensional conicity. The ω value is

assumed to be unity to simplify calculations. Furthermore, introducing a non-dimensional form of the harmonic solution, i.e. $\bar{w}(\bar{x}, \bar{t}) = \bar{W}(\bar{x})e^{-i\eta\bar{t}}$, and substituting this solution into Equation (31), the differential equation can be converted into the spatial domain as follows:

$$\frac{\partial^2}{\partial \bar{x}^2} \left[(1 + \bar{c}\bar{x})^3 \frac{\partial^2 \bar{W}(\bar{x})}{\partial \bar{x}^2} \right] - \eta^2 (1 + \bar{c}\bar{x}) \bar{W}(\bar{x}) = 0 \quad (32)$$

Here, $\eta = \frac{\omega}{\omega_n}$, also referred to as the frequency ratio, and $\bar{W}(\bar{x})$ represents the non-dimensional form of displacement amplitude. To address Equation (32), solutions based on Bessel functions, as defined in Equation (4), are employed. To derive the tower's DSM, the state vectors – rotation, bending moment, and shear force – are considered from Equation (5). Utilizing the

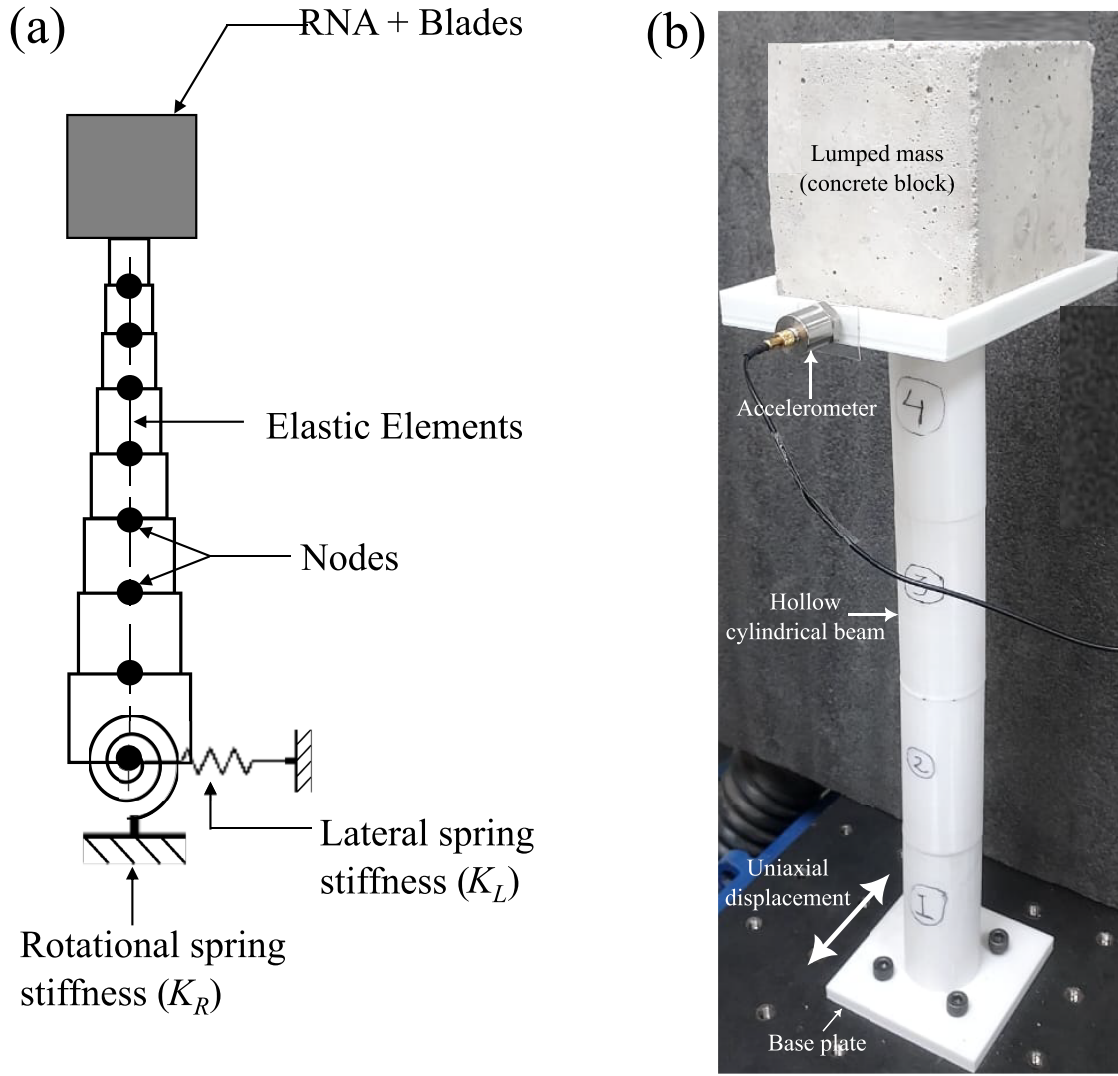


Figure 12. (a) Discretization of wind turbine system using OpenSEES ($n = 500$); (b) Reduced scaled model of a wind turbine tower. (This figure is available in colour online.)

aforementioned non-dimensional parameters, the state vectors in Equation (5) can be expressed in non-dimensional terms as follows:

$$\begin{aligned}\bar{\theta}(\bar{x}, \bar{t}) &= \theta_t(x, t)H_t = \frac{\partial \bar{W}(\bar{x})}{\partial \bar{x}} e^{-i\eta \bar{t}}, \quad \bar{M}(\bar{x}, \bar{t}) = M_t(x, t) \\ \frac{H_t^2}{E_t I_t(x)} &= \frac{\partial^2 \bar{W}(\bar{x})}{\partial \bar{x}^2} e^{-i\eta \bar{t}}, \\ \bar{V}(\bar{x}, \bar{t}) &= V_t(x, t) \frac{H_t^3}{E_t I_t(x)} = \left(\eta_c(\bar{x}) \frac{\partial^2 \bar{W}(\bar{x})}{\partial \bar{x}^2} + \frac{\partial^3 \bar{W}(\bar{x})}{\partial \bar{x}^3} \right) e^{-i\eta \bar{t}}\end{aligned}\quad (33)$$

Here, $\eta_c(\bar{x}) = \frac{3\bar{c}}{1+\bar{c}\bar{x}}$ represents the conicity ratio. By substituting the non-dimensional form of Equations (4) into (33), and then expressing the non-dimensional forms of Equations (6) and (7) in matrix form for the transverse direction, the DSM for the tower in the transverse direction can be obtained. To account for the

effect of the lumped mass in the DSM, the shear forces at the top of the tower can be defined as follows:

$$\begin{aligned}\left(V_t(x, t) - M_R \frac{\partial^2 w_t(x, t)}{\partial t^2} \right) \Big|_{x=0} &= 0 \\ \Rightarrow \bar{V}(\bar{x}, \bar{t}) \Big|_{\bar{x}=0} &= -\gamma \frac{\partial^2 \bar{w}(\bar{x}, \bar{t})}{\partial \bar{t}^2} \Big|_{\bar{x}=0}\end{aligned}\quad (34)$$

Here, $\gamma = \frac{M_R}{2\pi r_t \tau H_t \rho_t}$ is the ratio of the mass of the RNA to that of the mass of the tower. Similarly, the effect of lateral and rotational spring stiffness can be incorporated at the bottom of the tower as follows:

$$\begin{aligned}(M_t(x, t) - K_R \theta_t(x, t)) \Big|_{x=H_t} &= 0 \Rightarrow \bar{M}(\bar{x}, \bar{t}) \Big|_{\bar{x}=1} \\ &= \kappa_R \bar{\theta}(\bar{x}, \bar{t}) \Big|_{\bar{x}=1}\end{aligned}\quad (35)$$

and,

$$(V_t(x, t) + K_L w_t(x, t))|_{x=H_t} = 0 \Rightarrow \bar{V}(\bar{x}, \bar{t})|_{\bar{x}=1} = -\kappa_L \bar{w}(\bar{x}, \bar{t})|_{\bar{x}=1} \quad (36)$$

where K_L and K_R denote the lateral and rotational spring stiffness coefficients, respectively, which primarily depend on the geometric and material properties of the monopile and soil. A closed-form expression for K_L and K_R as a function of the geometric and material properties of the monopile and the soil are derived in the subsequent subsections. Additionally, $\kappa_L = \frac{K_L \omega L^3}{\pi E r_i^3 (1+c)^3 \tau}$ and $\kappa_R = \frac{K_R L}{\pi E r_i^3 (1+c)^3 \tau}$ represent the non-dimensional forms of spring coefficients, commonly known as the lateral stiffness ratio and rotational stiffness ratio, respectively. Now, by substituting the boundary conditions derived from Equations (34) to (36) at both ends of the beam into Equation (33), the non-dimensional form of the SEM can be modified as follows:

$$S_t = \begin{bmatrix} S_{t_{11}} - \gamma \eta^2 & S_{t_{21}} & S_{t_{31}} & S_{t_{14}} \\ S_{t_{21}} & S_{t_{22}} & S_{t_{23}} & S_{t_{24}} \\ S_{t_{31}} & S_{t_{32}} & S_{t_{33}} - k_L & S_{t_{34}} \\ S_{t_{14}} & S_{t_{42}} & S_{t_{43}} & S_{t_{44}} + k_R \end{bmatrix} \quad (37)$$

Now, eigenvalue analysis can be performed by equating the determinant of S_t to zero. The subsequent subsection outlines a procedure to obtain a closed-form expression of the lateral stiffness K_L as a function of the geometric and material properties of the monopile and the soil.

5.1. Expression for lateral spring stiffness

To obtain a closed-form expression of lateral spring stiffness (K_L), the monopile is subjected to static load (P_{ss}), and the corresponding deflection is calculated. The closed-form expression of K_L as a function of the physical properties of monopile and soil can be expressed as follows:

$$K_L = \frac{E_p I_p \lambda_{ss}^3 \{\cos(\lambda_{ss} H_s) \cosh(\lambda_{ss} H_s) - 1\}}{\cos(\lambda_{ss} H_s) \sinh(\lambda_{ss} H_s) - \cosh(\lambda_{ss} H_s) \sin(\lambda_{ss} H_s)} \quad (38)$$

where, $\lambda_{ss} = \sqrt{4 \frac{-(k_s + ic_s)}{E_p I_p}}$. The entire derivation for the expression of K_L is given in Appendix 1. Similarly, the next subsection outlines a procedure to obtain a closed-form expression of the rotational stiffness (K_R).

5.2. Expression for rotational spring stiffness

Similarly, to obtain the closed-form expression of the rotational spring stiffness (K_R) as a function of geometric

and material properties of the monopile and the soil, the monopile is subjected to static moment (M_{ss}) at the top and the corresponding deflection is calculated. The closed-form expression can be obtained as follows:

$$K_R = \frac{E_p I_p \lambda_{ss} \{\cos(\lambda_{ss} H_s) \cosh(\lambda_{ss} H_s) - 1\}}{\cos(\lambda_{ss} H_s) \sinh(\lambda_{ss} H_s) + \cosh(\lambda_{ss} H_s) \sin(\lambda_{ss} H_s)} \quad (39)$$

The entire derivation for the expression of K_R is given in Appendix 2. The subsequent subsections simplify the model shown in Figure 11 into a single degree of freedom system to derive a closed-form approximate expression of the natural frequency.

6. Approximate closed-form expression of natural frequency

This subsection outlines the derivation of an approximate expression for the natural frequency, following the methodology given in Adhikari and Bhattacharya (2011). The simplified mathematical model depicted in Figure 11 is converted into an equivalent Single Degree of Freedom (SDOF) system, characterised by equivalent stiffness (K_e) and equivalent mass (M_e). For this equivalent SDOF system, the first natural frequency is expressed as follows:

$$\omega_1 = \sqrt{\frac{K_e}{M_e}} \quad (40)$$

The equivalent mass can be obtained for a uniform cantilever beam carrying a tip mass from Blevins and Plunkett (1980) as follows:

$$M_e = M_R + 0.24 \rho_t A_t(x) H_t \quad (41)$$

The factor 0.24 on the right-hand side of Equation (41) can be replaced by the mass correction factor (γ_m) because the tower is non-uniform along its length and has elastic supports. Henceforth, the natural frequency of the system can be expressed as follows:

$$\omega_1 = \sqrt{\frac{K_e}{M_e}} = \sqrt{\frac{K_e}{M_R + \rho_t \Lambda H_t}} \quad (42)$$

where $\Lambda = 2\pi r_t \tau \gamma_m$ bearing the units of the cross-sectional area, also known as the equivalent area. Further sub-subsections derive the closed-form expression for equivalent stiffness and equivalent mass.

6.1. Equivalent stiffness

The equivalent stiffness (K_e) can be obtained by applying a static load (P_s) at the beam's free end and

calculating its corresponding deflection similar to the methodology discussed in Subsection 5.1. The closed-form expression of K_e can be defined as follows:

$$K_e = \frac{\pi E_t r_t^3 \tau}{H_t^3} \gamma_k \quad (43)$$

where γ_k is the stiffness correction factor defined as follows:

$$\gamma_k = \frac{\Omega_1}{\Omega_2 + \Omega_3 - \Omega_4 + \Omega_5} \quad (44)$$

where, $\Omega_1 = \frac{6\bar{c}^4 \kappa_L \kappa_R (\bar{c}+1)^4}{1+\bar{c}}$, $\Omega_2 = 2\bar{c}^3 \kappa_R (1-2\bar{c})$, $\Omega_3 = \frac{6\bar{c}^4 (\bar{c}+1)(\kappa_L + \kappa_R)}{1+\bar{c}}$, $\Omega_4 = \frac{3\bar{c} \kappa_L \kappa_R (2\bar{c}+7\bar{c}^2+8\bar{c}^3+3\bar{c}^4)}{1+\bar{c}}$ and $\Omega_5 = \frac{6\bar{c} \kappa_L \kappa_R \ln(\bar{c}+1)(1+4\bar{c}+6\bar{c}^2+4\bar{c}^3+\bar{c}^4)}{1+\bar{c}}$. The entire derivation of K_e is given in Appendix 3.

6.2. Equivalent mass

The equivalent mass (M_e) can be obtained by providing a unit displacement amplitude at the free end of the beam such that $(w(x, t)|_{x=0} = 1)$ and calculating its corresponding kinetic energy. The closed-form expression of M_e can be defined as follows:

$$M_e = \rho_t \Lambda H_t + M_R \quad (45)$$

where $\Lambda = 2\pi r_t \tau \gamma_m$ and the mass correction factor (γ_m) can be defined as follows:

$$\gamma_m = \frac{\Omega_6 + \Omega_7 + \frac{3\bar{c} \kappa_L \kappa_R \Omega_8}{1+\bar{c}}}{\Omega_9} \quad (46)$$

where, $\Omega_6 = \frac{9}{2} \kappa_R^2 \left(1 + \frac{6\bar{c}}{1+\bar{c}} + \frac{36\bar{c}^2}{(1+\bar{c})^2}\right) (2 + \bar{c})$, $\Omega_7 = \frac{27\bar{c}^2 \kappa_L^2}{(1+\bar{c})^2} (1 + \frac{\bar{c}}{4})$, $\Omega_8 = 9 + 3\bar{c} + \frac{9\bar{c}(3+\bar{c})}{1+\bar{c}} + \frac{3\bar{c} \kappa_L}{20(1+\bar{c})} (33 + 7\bar{c}) + 3\kappa_R \left(\frac{3\bar{c}}{1+\bar{c}} + 1\right) \left(\frac{3}{4} + \frac{\bar{c}}{5}\right) + \frac{3\kappa_L \kappa_R \bar{c}}{20(1+\bar{c})} \left(\frac{33}{7} + \frac{7}{8}\bar{c}\right)$ and $\Omega_9 = 3\kappa_R + \frac{9\bar{c} \kappa_L}{1+\bar{c}} + \frac{9\bar{c} \kappa_R}{1+\bar{c}} + \frac{3\bar{c} \kappa_L \kappa_R}{1+\bar{c}}$.

6.3. Closed form expression of natural frequency

Now, substituting the expression of equivalent stiffness (K_e) and equivalent mass (M_e) from Equations (43) and (45) in (42), the closed-form expression of natural frequency as a function of non-dimensional conicity (\bar{c}), lateral stiffness ratio (κ_L), rotational stiffness ratio (κ_R) and mass ratio (γ) can be derived as follows:

$$\omega_1^2 = \omega_n^2 \delta^2 \quad (47)$$

Here, $\delta = \sqrt{\frac{\gamma_k}{\gamma + \gamma_m}}$ serves as a frequency ratio of the SDOF system. This closed-form expression is validated against existing literature across various boundary conditions, as detailed in the subsequent sections on results and discussion.

6.4. Analytical validation

The validity of the proposed closed-form approximate expression for natural frequency, as outlined in Equation (47), is compared against existing literature across various boundary conditions. The following sub-subsections present this validation process.

6.4.1. Uniform beam having fixed support

The non-dimensional conicity parameter (\bar{c}) tends to zero for uniform cross-sections. In contrast, for fixed supports, the lateral stiffness ratio (κ_L) and rotational stiffness ratio (κ_R) tend towards infinity. Consequently, the formulations for the equivalent stiffness (K_e) and equivalent mass (M_e) defined in Equations (43) and (45) can be modified as follows:

$$\lim_{\bar{c} \rightarrow 0, \kappa_L \rightarrow \infty, \kappa_R \rightarrow \infty} K_e = \frac{3E_t I_t}{H_t^3} \quad (48)$$

and,

$$\lim_{\bar{c} \rightarrow 0, \kappa_L \rightarrow \infty, \kappa_R \rightarrow \infty} M_e = M_R + \frac{33}{140} \rho_t A_t H_t \quad (49)$$

Equations (48) and (49) are the exact expressions of equivalent stiffness and equivalent mass for a cantilever beam connected by a lumped mass at the free end, which agrees exactly with Table 8 of Blevins and Plunkett (1980).

6.4.2. Uniform beam having flexible support

For $\bar{c} = 0$, the stiffness (γ_k) and mass correction factor (γ_m) defined in Equations (44) and (46) can be modified as follows:

$$\lim_{\bar{c} \rightarrow 0} (\gamma_k) = \frac{3\kappa_L \kappa_R}{3\kappa_L 3\kappa_R + \kappa_L \kappa_R} \quad (50)$$

and,

$$\lim_{\bar{c} \rightarrow 0} (\gamma_m) = \frac{3}{140} \times \frac{140\kappa_L^2 + 420\kappa_R^2 + 420\kappa_L \kappa_R + 77\kappa_L^2 \kappa_R + 105\kappa_R^2 \kappa_L + 11\kappa_L^2 \kappa_R^2}{(3\kappa_L + 3\kappa_R + \kappa_L \kappa_R)^2} \quad (51)$$

Equations (50) and (51) is the exact expression of equivalent stiffness and equivalent mass provided in Equation (71) of Adhikari and Bhattacharya (2011). The subsequent section provides a detailed analysis to obtain the natural frequency of a wind turbine tower using a numerical approach.

6.5. Numerical validation

The finite element software Open System for Earthquake Engineering Simulation (OpenSEES) (McKenna

2011) has been used to validate the proposed mathematical model. In this software, a numerical model based on the finite element method is developed, and an eigenvalue analysis is performed to estimate the natural frequency of the wind turbine system. Like the mathematical model, a heavy mass is considered at the top to represent the RNA and the blades. To model the conical tower, it is discretised into n cylindrical continuous beam elements made of an elastic material with a constant cross-section (Arany, Bhattacharya, Adhikari et al. 2015), as shown in Figure 12(a). For SSI, lateral and rotational springs are attached at the bottom node of the lowest element using zero-length elements. The natural frequencies obtained from the finite element simulations are compared with those from analytical methods and are presented in Table 3. The next section outlines an experimental validation using a reduced-scale model to determine the natural frequency.

6.6. Experimental validation

As shown in Figure 12(b), the experimental setup consists of a hollow cylindrical tower fixed at the bottom plate, with a heavy lumped mass placed at the top. The hollow cylindrical tower has been 3D-printed using PLA material. The geometric and material properties of all components are provided in Table 2. The bottom plate is allowed to move unilaterally, creating a sudden displacement or jerk, which induces free-damped vibration in the system. A uniaxial accelerometer (Neeshpapa et al. 2014) is attached to the tip of the tower, as shown in Figure 12(b), to record the system's acceleration amplitude. The technical specifications of the accelerometer are provided in Table 2. The accelerometer is connected to a data acquisition (DAQ) system, which interfaces with a PC to obtain the time-domain response via LabView software (Kalkman 1995). The recorded vertical acceleration vs. time data is then transformed into the frequency domain using the Fast Fourier Transform (FFT) algorithm (Duhamel and Vetterli

Table 2. Geometric and material properties of the experimental model shown in Figure 12(b).

Apparatus	Properties	Symbols	Units	Values
PLA material	Density	ρ	kg/m ³	778.89
	Young's modulus	E	GPa	2.9
Tower	Height	H	m	0.4
	Outer diameter	D	m	0.04
	Thickness	τ_p	m	0.002
Rigid mass	Mass	M_r	kg	2
Accelerometer	Sensitivity	—	mV/(m/s ²)	4.98
	Mass	M_a	kg	0.0236
Natural Frequency	Experiment	ω_e	Hz	7.2
	Bessel function solution (Error %)	ω_b	Hz	7.15 (0.694 %)
	Approximate solution (Error %)	ω_1	Hz	7.26 (0.83 %)
	Numerical simulation (Error %)	ω_n	Hz	7.31 (1.52 %)

Table 3. Physical properties and natural frequency results for four different wind turbines.

Components		Vestas V90 3 MW (Romero et al. 2016)	Vestas V66 2 MW (Almutairi and Alahmadi 2022)	NREL 5 MW (Jonkman et al. 2009)	Siemens SWT 3.6 MW (Pangerc et al. 2016)
Tower	Length, H_t (m)	80	54.5	90	60
	Top outside diameter, D_{tt} (m)	2.31	2.75	3.87	2.8
	Bottom outside diameter, D_{tb} (m)	4.2	4.25	6	3.5
	Wall thickness, τ (mm)	30	34	23	47.5
	Young's modulus, E_t (GPa)	210	210	210	210
	Density, ρ_t (kg/m ³)	7850	7860	8500	8500
	RNA mass, M_R (tonne)	111	80	350	130
Monopile	Length, H_p (m)	28	31.5	56	71
	Outside diameter, D_p (m)	4.3	3.5	6	3.5
	Wall thickness, t_p (mm)	45	50	60	75
	Density, ρ_p (kg/m ³)	7850	7860	8500	8500
	Young's modulus, E_p (GPa)	210	210	210	210
	Mean sea depth, H_f (m)	8	16.5	20	21
	Young's modulus, E_s (MPa)	20	5160	158.46	105.64
Soil	Density, ρ_s (kg/m ³)	1500	2850	1019.36	1019.36
	Poisson's ratio, μ_s	0.3	0.2	0.3205	0.3205
Natural frequency (Hz)	Real-world MSWT	0.28–0.35	0.69–0.77	0.22–0.32	0.4–0.6
	Bessel function solution	0.307	0.737	0.26	0.452
	Approximate solution	0.297	0.729	0.258	0.451
	Error (%)	3.016	0.985	0.502	0.079
	Fixed base condition	0.347	0.809	0.277	0.517
	Flexibility (%)	11.527	8.899	6.137	12.572

1990). The peak amplitude in the FFT graph corresponds to the system's natural frequency. The natural frequency obtained from the experiment is validated against numerical and analytical methods, as shown in Table 2. Further details on the experimental procedures can be found in Patro, Banerjee et al. (2023). The subsequent section compares the natural frequencies obtained from Equation (47) with the complete analytical model discussed in Section 5 for different real-world MSWTs.

7. Application of the methodology to installed wind turbines and discussion

This section undertakes a comparison between the natural frequencies derived from the empirical formula outlined in Equation (47) and those obtained from the comprehensive analytical model detailed in Equation (5), focussing on different types of MSWTs found in various global wind farms. Specifically, four distinct MSWT case models are considered, encompassing a total of 16 input parameters that encompass the physical characteristics of the tower, monopile, and site conditions. These parameters collectively contribute to calculating natural frequencies using both the empirical formula and the comprehensive analytical approach, as outlined in Table 3. The findings reveal a remarkable alignment between the natural frequencies predicted by the empirical formula and the measured frequencies, typically within a 3.1% margin. This level of accuracy is noteworthy, considering the simplified nature of the methodology employed. Furthermore, when comparing the fixed base and natural frequencies to those incorporating flexible foundations using our method, the disparity typically falls within the range of 6–13%, a common occurrence in offshore wind turbine analyses. The degree of flexibility introduced by the foundation's compliance, expressed as a percentage reduction in the first natural frequency, is documented for each wind turbine model in Table 3.

8. Conclusion

This study utilises a frequency domain dynamic stiffness approach to investigate the dynamic response of a monopile-supported offshore wind turbine (MSWT) under ship impact loading. In this analysis, the tower and monopile are modelled as Euler-Bernoulli beams. Fluid-structure interaction (FSI) is accounted for by applying hydrodynamic mass along the entire submerged length of the monopile. Similarly, soil-structure interaction (SSI) is modelled using viscoelastic springs distributed along the length of the monopile embedded within the soil. The force-displacement relationship for the combined system of the tower and monopile is established through the Spectral Element Method (SEM).

The dynamic response at the top of the tower in the frequency domain is evaluated when subjected to impact loading at its base. A parametric study demonstrates how the dynamic response at the top varies with changes in the ship's mass, impact velocity, and water depth. It was found that the maximum dynamic response consistently occurs at the resonant frequency of the MSWT across all scenarios. Consequently, a sensitivity analysis using the Pearson correlation was conducted to assess the influence of various geometric and material parameters of the tower, monopile, and soil on the system's natural frequency. This analysis revealed that the mass of the rotor nacelle assembly (RNA) (M_R) and the bottom diameter of the tower (D_{tb}) are significantly sensitive to changes in the natural frequency, underscoring their importance in the MSWT design process. Conversely, the depth of the monopile submerged in water (H_f) showed a negligible impact on the natural frequency.

A simplified non-dimensional model was proposed to account for the non-uniform geometry of the system, and the foundation was modelled using lateral and rotational springs. Closed-form expressions for these springs have been derived based on the physical properties of the monopile and soil. An analytical approximate closed-form expression for the natural frequency has been formulated, facilitating the preliminary design of beam-like structures considering their conicity and flexible supports. This expression enables manual natural frequency estimation and simplifies dynamic analysis for hollow conical Euler-Bernoulli beams with similar structural configurations. By reverse engineering, the geometric parameters of the wind turbine can be recalculated based on a desired natural frequency. The proposed model effectively captures the dynamic response of MSWTs under varying impact energies and deformation modes from local indentations to global bending and incorporates foundation and geometric effects for diverse design scenarios. The major limitation of the present study is that a linear elastic model is considered for the tower, monopile, and soil. The large deformations of the structure, material, and geometric nonlinearity can be considered in future work. Additionally, future work may extend to estimating stochastic dynamic responses, considering the dynamics of the rotating blades.

Author contributions

CRedit: **Somya Ranjan Patro**: Conceptualization, Data curation, Formal analysis, Methodology, Writing – original draft; **Arnab Banerjee**: Funding acquisition, Supervision, Writing – review & editing; **Sondipon Adhikari**: Supervision, Writing – review & editing; **G. V. Ramana**: Supervision, Writing – review & editing.

Disclosure statement

The authors declare that they have no known competing financial interests or personal relationships that could have appeared to influence the work reported in this paper.

Funding

The authors would like to acknowledge the research grant, namely: Core research grant, Science and Engineering Research Board, Department of Science and Technology (DST), Ministry of Science and Technology, Government of India, Grant number CRG/2019/004696. Scheme for Promotion of Academic and Research Collaboration, Ministry of Human Resource Development, Government of India, Grant number SPARC/2019-2020/P1715/SL.

ORCID

Somya Ranjan Patro  <http://orcid.org/0000-0001-8607-9765>

Data availability statement

No data was used for the research described in the article.

References

- Adhikari S, Bhattacharya S. 2011. Vibrations of wind-turbines considering soil-structure interaction. *Wind Struct Int J*. 14(2):85-112. doi: [10.12989/was.2011.14.2.085](https://doi.org/10.12989/was.2011.14.2.085)
- Adhikari S, Bhattacharya S. 2012. Dynamic analysis of wind turbine towers on flexible foundations. *Shock Vib*. 19(1):37-56. doi: [10.1155/2012/408493](https://doi.org/10.1155/2012/408493)
- Adhikari S, Bhattacharya S. 2021. A general frequency adaptive framework for damped response analysis of wind turbines. *Soil Dyn Earthquake Eng*. 143:106605. doi: [10.1016/j.soildyn.2021.106605](https://doi.org/10.1016/j.soildyn.2021.106605)
- Ahmed V, Saboor S, Alshamsi HA, Almarzooqi FA, Alketbi MA, Al Marei FA. 2024. Net-zero energy buildings and the sustainable development goals. In: *The Elgar companion to the built environment and the sustainable development goals*. Sharjah: Edward Elgar Publishing; p. 196-216.
- Alkhoury P, Soubra A-H, Rey V, A-Ahmed M. 2021. A full three-dimensional model for the estimation of the natural frequencies of an offshore wind turbine in sand. *Wind Energy*. 24(7):699-719. doi: [10.1002/we.v24.7](https://doi.org/10.1002/we.v24.7)
- Almutairi K, Alahmadi R. 2022. The feasibility of the first utility-scale wind farm in Saudi Arabia (the 400 MW Dumat Al-Jandal project). *J Clean Energy Technol*. 10(1):1-10. doi: [10.18178/JOCET](https://doi.org/10.18178/JOCET)
- Anil Bindu A, Thampatty KS. 2024. Repowering feasibility of indian wind energy sector: a case study. *Wind Eng*. 48(5):911-937. doi: [10.1177/0309524X241238244](https://doi.org/10.1177/0309524X241238244)
- Arany L, Bhattacharya S, Adhikari S, Hogan S, Macdonald JHG. 2015. An analytical model to predict the natural frequency of offshore wind turbines on three-spring flexible foundations using two different beam models. *Soil Dyn Earthquake Eng*. 74:40-45. doi: [10.1016/j.soildyn.2015.03.007](https://doi.org/10.1016/j.soildyn.2015.03.007)
- Arany L, Bhattacharya S, Macdonald J, Hogan SJ. 2015. Simplified critical mudline bending moment spectra of offshore wind turbine support structures. *Wind Energy*. 18(12):2171-2197. doi: [10.1002/we.v18.12](https://doi.org/10.1002/we.v18.12)
- Arany L, Bhattacharya S, Macdonald JH, Hogan SJ. 2016. Closed form solution of Eigen frequency of monopile supported offshore wind turbines in deeper waters incorporating stiffness of substructure and SSI. *Soil Dyn Earthquake Eng*. 83:18-32. doi: [10.1016/j.soildyn.2015.12.011](https://doi.org/10.1016/j.soildyn.2015.12.011)
- Bela A, Le Sourne H, Buldgen L, Rigo P. 2017. Ship collision analysis on offshore wind turbine monopile foundations. *Mar Struct*. 51:220-241. doi: [10.1016/j.marstruc.2016.10.009](https://doi.org/10.1016/j.marstruc.2016.10.009)
- Bhattacharya S. 2019. *Design of foundations for offshore wind turbines*. Swansea (UK): John Wiley & Sons.
- Bisoi S, Haldar S. 2019. 3D modeling of long-term dynamic behavior of monopile-supported offshore wind turbine in clay. *Int J Geomech*. 19(7):04019062. doi: [10.1061/\(ASCE\)GM.1943-5622.0001437](https://doi.org/10.1061/(ASCE)GM.1943-5622.0001437)
- Blevins RD, Plunkett R. 1980. Formulas for natural frequency and mode shape. *J Appl Mech*. 47(2):461. doi: [10.1115/1.3153712](https://doi.org/10.1115/1.3153712)
- Boiangiu M, Ceausu V, Untaroiu CD. 2016. A transfer matrix method for free vibration analysis of Euler-Bernoulli beams with variable cross section. *J Vib Control*. 22(11):2591-2602. doi: [10.1177/1077546314550699](https://doi.org/10.1177/1077546314550699)
- Bouzid DA, Bhattacharya S, Otsmane L. 2018. Assessment of natural frequency of installed offshore wind turbines using nonlinear finite element model considering soil-monopile interaction. *J Rock Mech Geotech Eng*. 10(2):333-346. doi: [10.1016/j.jrmge.2017.11.010](https://doi.org/10.1016/j.jrmge.2017.11.010)
- Bowman F. 2012. *Introduction to Bessel functions*. New York (NY): Courier Corporation.
- Bozyigit B, Bozyigit I, Prendergast LJ. 2023. Analytical approach for seismic analysis of onshore wind turbines considering soil-structure interaction. *Struct*. 51:226-241. <https://doi.org/10.1016/j.istruc.2023.03.048>.
- Broersen A. 2020. *Analytical model to assess bending moments in wind turbine support structures subjected to ship collisions [Master's thesis]*. NTNU.
- Colherinhas GB, de Moraes MVG, Machado MR. 2022. Spectral model of offshore wind turbines and vibration control by pendulum tuned mass dampers. *Int J Struct Stab Dyn*. 22(05):2250053. doi: [10.1142/S0219455422500535](https://doi.org/10.1142/S0219455422500535)
- Cook RD. 2007. *Concepts and applications of finite element analysis*. New Jersey (NJ): John Wiley & Sons.
- Damgaard M, Andersen JK. 2012. Natural frequency and damping estimation of an offshore wind turbine structure. In: *ISOPE International Ocean and Polar Engineering Conference*. ISOPE; p. ISOPE-I.
- Darvishi Alamouti S, Bahaari M, Moradi M. 2020. Dynamic analysis of a monopile supported wind turbine considering experimental p - y curves. *Ships offshore Struct*. 15(6):670-682. doi: [10.1080/17445302.2019.1665910](https://doi.org/10.1080/17445302.2019.1665910)
- Darvishi-Alamouti S, Bahaari M-R, Moradi M. 2017. Natural frequency of offshore wind turbines on rigid and flexible monopiles in cohesionless soils with linear stiffness distribution. *Appl Ocean Res*. 68:91-102. doi: [10.1016/j.apor.2017.07.009](https://doi.org/10.1016/j.apor.2017.07.009)
- Das A, Banerjee A, Bera KK. 2024. Bending-bending-torsion coupled wave propagation in thin-walled asymmetric meta-beam: an analytical and experimental analysis. *Thin-Walled Struct*. 198:111737. doi: [10.1016/j.tws.2024.111737](https://doi.org/10.1016/j.tws.2024.111737)
- Das R, Banerjee A, Manna B. 2023. Estimation of the dissipation due to radiation damping for the pile embedded in soil: a closed-form solution. *Comput Geotech*. 163:105716. doi: [10.1016/j.compgeo.2023.105716](https://doi.org/10.1016/j.compgeo.2023.105716)

- Das R, Manna B, Banerjee A. 2023. Spectral element formulation for rock-socketed mono-pile under horizontal dynamic loads. *Soil Dyn Earthquake Eng.* 169:107863. doi: [10.1016/j.soildyn.2023.107863](https://doi.org/10.1016/j.soildyn.2023.107863)
- Das R, Patro SR, Manna B, Ramana G, Banerjee A. 2024. Resonator-impregnated monopile-supported wind turbine system: an experimental investigation of dynamic vibration control. *J Geotech Geoenviron Eng.* 150(11):04024109. doi: [10.1061/JGGEFK.GTENG-12630](https://doi.org/10.1061/JGGEFK.GTENG-12630)
- Demirci HE, Jalbi S, Bhattacharya S. 2022. Liquefaction effects on the fundamental frequency of monopile supported offshore wind turbines (OWTs). *Bull Earthquake Eng.* 20(7):3359–3384. doi: [10.1007/s10518-022-01360-9](https://doi.org/10.1007/s10518-022-01360-9)
- Deng R, Zhou X-H, Ji W-D, Li R-F, Zheng S-Q, Wang Y-H. 2023. Coupled behaviour and strength prediction of tapered cfdst columns with large hollow ratios for wind turbine towers. *Eng Struct.* 289:116287. doi: [10.1016/j.engstruct.2023.116287](https://doi.org/10.1016/j.engstruct.2023.116287)
- Derucher K. 1982. Analysis of concrete bridge piers for vessel impact. *Civ Eng Pract Des Eng.* 1:393–420.
- DNV GL AS Oslo. 2016. Machinery for wind turbines. In: Standard DNVGL-ST-0361. Norway: DNV GL AS Oslo; p. 16–31.
- Duhamel P, Vetterli M. 1990. Fast fourier transforms: a tutorial review and a state of the art. *Signal Process.* 19(4):259–299. doi: [10.1016/0165-1684\(90\)90158-U](https://doi.org/10.1016/0165-1684(90)90158-U)
- Echeverry S, Le Sourné H, Bela A, Pire T, Rigo P. 2017. Design methods to assess the resistance of offshore wind turbine structures impacted by a ship. In: *Proceedings of the 7th European African Conference on Wind Engineering*, Liege, Belgium. p. 15–18.
- Ferreira YA, Vernizzi GJ, Futai MM, Franzini GR. 2022. A reduced-order model to predict the natural frequencies of offshore wind turbines considering soil–structure interaction. *Mar Syst Ocean Technol.* 17(2):80–94. doi: [10.1007/s40868-022-00116-z](https://doi.org/10.1007/s40868-022-00116-z)
- Freedman B. 2024. renewable and non-renewable energy sources. *Environ Sci.* 5:672.
- Gander W, Hrebicek J. 2004. Solving problems in scientific computing using MAPLE and MATLAB®. Berlin: Springer Science & Business Media.
- Gao D, Zhang C. 2021. Dynamic behavior of jacket foundation for offshore wind turbine subjected to ship impact. In: *EASEC16: Proceedings of The 16th East Asian-Pacific Conference on Structural Engineering and Construction*, 2019. Springer; p. 719–729.
- Goyal A, Chopra AK. 1989. Simplified evaluation of added hydrodynamic mass for intake towers. *J Eng Mech.* 115(7): 1393–1412. doi: [10.1061/\(ASCE\)0733-9399\(1989\)115:7\(1393\)](https://doi.org/10.1061/(ASCE)0733-9399(1989)115:7(1393))
- Gu C, Chen D, Liu F, Fang K, Guo D, Marzocca P. 2021. Dynamic analysis of flexible wind turbine tower by a transfer matrix method. *Int J Struct Stab Dyn.* 21(10):2150142. doi: [10.1142/S021945542150142X](https://doi.org/10.1142/S021945542150142X)
- Gücüyen E. 2017. Analysis of offshore wind turbine tower under environmental loads. *Ships offshore Struct.* 12(4):513–520. doi: [10.1080/17445302.2016.1181027](https://doi.org/10.1080/17445302.2016.1181027)
- Hao E, Liu C. 2017. Evaluation and comparison of anti-impact performance to offshore wind turbine foundations: monopile, tripod, and jacket. *Ocean Eng.* 130:218–227. doi: [10.1016/j.oceaneng.2016.12.008](https://doi.org/10.1016/j.oceaneng.2016.12.008)
- Hsieh J-R. 2015. Analytical formulations for ship-offshore wind turbine collisions [Master's thesis]. Belgique: Université de Liège, Liège.
- Isherwood R. 1987. A revised parameterisation of the Jonswap spectrum. *Appl Ocean Res.* 9(1):47–50. doi: [10.1016/0141-1187\(87\)90030-7](https://doi.org/10.1016/0141-1187(87)90030-7)
- Jahani K, Langlois RG, Afagh FF. 2022. Structural dynamics of offshore wind turbines: a review. *Ocean Eng.* 251:111136. doi: [10.1016/j.oceaneng.2022.111136](https://doi.org/10.1016/j.oceaneng.2022.111136)
- James M, Haldar S, Bhattacharya S. 2024. Impact of climate change on the design of multi-megawatt spar floating wind turbines. *Mar Struct.* 93:103547. doi: [10.1016/j.marstruct.2023.103547](https://doi.org/10.1016/j.marstruct.2023.103547)
- Jonkman J, Butterfield S, Musial W, Scott G. 2009. Definition of a 5-MW reference wind turbine for offshore system development. Golden, CO: National Renewable Energy Lab. (NREL). Technical report.
- Kaimal JC, Wyngaard J, Izumi Y, Coté O. 1972. Spectral characteristics of surface-layer turbulence. *Quart J Roy Meteorol Soc.* 98(417):563–589.
- Kalkman CJ. 1995. Labview: a software system for data acquisition, data analysis, and instrument control. *J Clin Monit.* 11(1):51–58. doi: [10.1007/BF01627421](https://doi.org/10.1007/BF01627421)
- Kleusberg E. 2017. Wind turbine simulations using spectral elements [PhD thesis]. KTH Royal Institute of Technology.
- Ko Y-Y. 2020. A simplified structural model for monopile-supported offshore wind turbines with tapered towers. *Renew Energy.* 156:777–790. doi: [10.1016/j.renene.2020.03.149](https://doi.org/10.1016/j.renene.2020.03.149)
- Kreyszig E. 2013. *Differential geometry*. Massachusetts (MA): Courier Corporation.
- Kreyszig E, Stroud K, Stephenson G. 2008. *Advanced engineering mathematics. Integration.* 9(4):1248.
- Ladeira I, Jaramillo SE, Le Sourné H. 2023. A simplified method to assess the elasto-plastic response of standalone tubular offshore wind turbine supports subjected to ship impact. *Ocean Eng.* 279:114313. doi: [10.1016/j.oceaneng.2023.114313](https://doi.org/10.1016/j.oceaneng.2023.114313)
- Ladeira I, Márquez L, Echeverry S, Le Sourné H, Rigo P. 2023. Review of methods to assess the structural response of offshore wind turbines subjected to ship impacts. *Ships offshore Struct.* 18(6):755–774. doi: [10.1080/17445302.2022.2072583](https://doi.org/10.1080/17445302.2022.2072583)
- Lee U. 2009. *Spectral element method in structural dynamics*. New Jersey (NJ): John Wiley & Sons.
- Le Sourné H, Pire T, Hsieh J, Rigo P. 2016. New analytical developments to study local and global deformations of an offshore wind turbine jacket impacted by a ship. In: *Proceedings of the 7th International Conference on Collision and Grounding of Ships and Offshore Structures (ICCGS'16)*. Korea: University of Ulsan Ulsan; p. 15–18.
- Leung AY. 2012. *Dynamic stiffness and substructures*. Berlin: Springer Science & Business Media.
- Liaw C-Y, Chopra AK. 1974. Dynamics of towers surrounded by water. *Earthq Eng Struct Dyn.* 3(1):33–49. doi: [10.1002/eqe.v3:1](https://doi.org/10.1002/eqe.v3:1)
- Liu Y, Li X, Shi W, Wang W, Jiang Z. 2024. Vibration control of a monopile offshore wind turbines under recorded seismic waves. *Renew Energy.* 226:120455. doi: [10.1016/j.renene.2024.120455](https://doi.org/10.1016/j.renene.2024.120455)
- Ma H, Yang J, Chen L. 2017. Numerical analysis of the long-term performance of offshore wind turbines supported by monopiles. *Ocean Eng.* 136:94–105. doi: [10.1016/j.oceaneng.2017.03.019](https://doi.org/10.1016/j.oceaneng.2017.03.019)
- McKenna F. 2011. Opensees: a framework for earthquake engineering simulation. *Comput Sci Eng.* 13(4):58–66. doi: [10.1109/MCSE.2011.66](https://doi.org/10.1109/MCSE.2011.66)

- Mehreganian N, Safa Y, Boiger GK. 2024. Impact analysis of wind turbines subjected to ship collision and blast loading. In: *Multiphysics of wind turbines in extreme loading conditions*. Amsterdam: Elsevier; p. 101–138.
- Meng W, Zhangqi W. 2011. The vibration frequencies of wind turbine steel tower by transfer matrix method. In: *2011 Third International Conference on Measuring Technology and Mechatronics Automation*. Vol. 3. IEEE; p. 995–998.
- Minorsky V. 1958. *An analysis of ship collisions with reference to protection of nuclear power plants*. New York: Sharp (George G.) Inc. Technical report.
- Moreno J, Campagnolo L, Boitier B, Nikas A, Koasidis K, Gambhir A, Gonzalez-Eguino M, Perdana S, Van de Ven D-J, Chiodi A, et al. 2024. The impacts of decarbonization pathways on sustainable development goals in the European Union. *Commun Earth Environ*. 5(1):136. doi: [10.1038/s43247-024-01309-7](https://doi.org/10.1038/s43247-024-01309-7)
- Moulas D, Shafee M, Mehmanparast A. 2017. Damage analysis of ship collisions with offshore wind turbine foundations. *Ocean Eng*. 143:149–162. doi: [10.1016/j.oceaneng.2017.04.050](https://doi.org/10.1016/j.oceaneng.2017.04.050)
- Moynihan B, Mehrjoo A, Moaveni B, McAdam R, Rüdinger F, Hines E. 2023. System identification and finite element model updating of a 6 MW offshore wind turbine using vibrational response measurements. *Renew Energy*. 219:119430. doi: [10.1016/j.renene.2023.119430](https://doi.org/10.1016/j.renene.2023.119430)
- Musial W, Spitsen P, Duffy P, Beiter P, Shields M, Mulas Hernando D, Hammond R, Marquis M, King J, Sathish S. 2023. *Offshore wind market report: 2023 edition*. Golden, CO: National Renewable Energy Laboratory (NREL). Technical report.
- Neeshpapa A, Antonov A, Agafonov V. 2014. A low-noise DC seismic accelerometer based on a combination of MET/MEMS sensors. *Sensors*. 15(1):365–381. doi: [10.3390/s150100365](https://doi.org/10.3390/s150100365)
- Nie Y, Fang H, Meng X. 2024. Ship collision mitigation for offshore wind turbine monopile foundations via high-general/low-collision-stiffness steel fenders. *Ocean Eng*. 299:117272. doi: [10.1016/j.oceaneng.2024.117272](https://doi.org/10.1016/j.oceaneng.2024.117272)
- Norén-Cosgriff K, Kaynia AM. 2021. Estimation of natural frequencies and damping using dynamic field data from an offshore wind turbine. *Mar Struct*. 76:102915. doi: [10.1016/j.marstruc.2020.102915](https://doi.org/10.1016/j.marstruc.2020.102915)
- Novak M. 1974. Dynamic stiffness and damping of piles. *Can Geotech J*. 11(4):574–598. doi: [10.1139/t74-059](https://doi.org/10.1139/t74-059)
- Novak M, Aboul-Ella F, Nogami T. 1978. Dynamic soil reactions for plane strain case. *J Eng Mech Div*. 104(4):953–959. doi: [10.1061/JMCEA3.0002392](https://doi.org/10.1061/JMCEA3.0002392)
- Panda S, Banerjee A, Baxy A, Manna B, Adhikari S. 2023. Artificial neural network-based multiple-input multiple-output metamodel for prediction of design parameters for a high-speed rail viaduct. *Struct Infrastruct Eng*. 21(1):1–15. doi: [10.1080/15732479.2023.2275698](https://doi.org/10.1080/15732479.2023.2275698)
- Pangerc T, Theobald PD, Wang LS, Robinson SP, Lepper PA. 2016. Measurement and characterisation of radiated underwater sound from a 3.6 MW monopile wind turbine. *J Acoust Soc Am*. 140(4):2913–2922. doi: [10.1121/1.4964824](https://doi.org/10.1121/1.4964824)
- Patro SR, Banerjee A, Ramana G. 2023. Vibration attenuation characteristics of finite locally resonant meta beam: theory and experiments. *Eng Struct*. 278:115506. doi: [10.1016/j.engstruct.2022.115506](https://doi.org/10.1016/j.engstruct.2022.115506)
- Patro SR, Panda S, Ramana G, Banerjee A. 2024. Optimal multiple tuned mass dampers for monopile supported offshore wind turbines using genetic algorithm. *Ocean Eng*. 298:117356. doi: [10.1016/j.oceaneng.2024.117356](https://doi.org/10.1016/j.oceaneng.2024.117356)
- Pedersen PT, Valsgaard S, Olsen D, Spangenberg S. 1993. Ship impacts: bow collisions. *Int J Impact Eng*. 13(2):163–187. doi: [10.1016/0734-743X\(93\)90091-K](https://doi.org/10.1016/0734-743X(93)90091-K)
- Pezeshki H, Pavlou D, Adeli H, Siriwardane SC. 2023. Modal analysis of offshore monopile wind turbine: an analytical solution. *J offshore Mech Arct Eng*. 145(1):010907. doi: [10.1115/1.4055402](https://doi.org/10.1115/1.4055402)
- Pezeshki H, Pavlou D, Siriwardane SC. 2024. Analytical estimation of natural frequencies of offshore monopile wind turbines. In: *Olympiad in engineering science*. Berlin: Springer; p. 421–436.
- Pire T, Le Sourne H, Echeverry S, Rigo P. 2018. Analytical formulations to assess the energy dissipated at the base of an offshore wind turbine jacket impacted by a ship. *Mar Struct*. 59:192–218. doi: [10.1016/j.marstruc.2018.02.002](https://doi.org/10.1016/j.marstruc.2018.02.002)
- Qin M, Shi W, Chai W, Fu X, Li L, Li X. 2023. Extreme structural response prediction and fatigue damage evaluation for large-scale monopile offshore wind turbines subject to typhoon conditions. *Renew Energy*. 208:450–464. doi: [10.1016/j.renene.2023.03.066](https://doi.org/10.1016/j.renene.2023.03.066)
- Rao SS. 2019. *Vibration of continuous systems*. New Jersey (NJ): John Wiley & Sons.
- Romero A, Lage Y, Soua S, Wang B, Gan T-H. 2016. Vestas v90-3 MW wind turbine gearbox health assessment using a vibration-based condition monitoring system. *Shock Vib*. 2016(1):1.18
- Shah IH, Manzoor MA, Jinhui W, Li X, Hameed MK, Rehaman A, Li P, Zhang Y, Niu Q, Chang L. 2024. Comprehensive review: effects of climate change and greenhouse gases emission relevance to environmental stress on horticultural crops and management. *J. Environ. Manage.*. 351:119978. doi: [10.1016/j.jenvman.2023.119978](https://doi.org/10.1016/j.jenvman.2023.119978)
- Song M, Jiang Z, Yuan W. 2021. Numerical and analytical analysis of a monopile-supported offshore wind turbine under ship impacts. *Renew Energy*. 167:457–472. doi: [10.1016/j.renene.2020.11.102](https://doi.org/10.1016/j.renene.2020.11.102)
- Wan J-H, Bai R, Li X-Y, Liu S-W. 2023. Natural frequency analysis of monopile supported offshore wind turbines using unified beam-column element model. *J Mar Sci Eng*. 11(3):628. doi: [10.3390/jmse11030628](https://doi.org/10.3390/jmse11030628)
- Wang K, Ji C, Xue H, Tang W. 2017. Frequency domain approach for the coupled analysis of floating wind turbine system. *Ships offshore Struct*. 12(6):767–774. doi: [10.1080/17445302.2016.1241365](https://doi.org/10.1080/17445302.2016.1241365)
- Wang P, Zhao M, Du X, Liu J, Xu C. 2018. Wind, wave and earthquake responses of offshore wind turbine on monopile foundation in clay. *Soil Dyn Earthquake Eng*. 113:47–57. doi: [10.1016/j.soildyn.2018.04.028](https://doi.org/10.1016/j.soildyn.2018.04.028)
- Yu Z, Amdahl J. 2023. A Rayleigh-Ritz solution for high order natural frequencies and eigenmodes of monopile supported offshore wind turbines considering tapered towers and soil pile interactions. *Mar Struct*. 92:103482. doi: [10.1016/j.marstruc.2023.103482](https://doi.org/10.1016/j.marstruc.2023.103482)
- Zhang Y, Hu Z. 2022. An aero-hydro coupled method for investigating ship collision against a floating offshore wind turbine. *Mar Struct*. 83:103177. doi: [10.1016/j.marstruc.2022.103177](https://doi.org/10.1016/j.marstruc.2022.103177)

Appendices

Appendix 1. Derivation for lateral spring stiffness

For a monopile subjected to static load (P_{ss}), the governing differential equation defined in Equation (20) can be modified as follows:

$$E_p I_p \frac{\partial^4 W_s(x_s)}{\partial x_s^4} + (k_s + i c_s) W_s(x_s) = 0 \quad (\text{A1})$$

The trigonometric hyperbolic solution for the above differential equation can be obtained similar to Equation (22) as follows:

$$W_s(x_s) = \mathbf{S}_s(x_s) \mathbf{F}_s \quad (\text{A2})$$

where,

$\mathbf{S}_s(x_s) = \begin{Bmatrix} \sin(\lambda_{ss} x_s) & \cos(\lambda_{ss} x_s) & \sinh(\lambda_{ss} x_s) & \cosh(\lambda_{ss} x_s) \end{Bmatrix}$ and $\mathbf{F}_s = \{F_{s1} \ F_{s2} \ F_{s3} \ F_{s4}\}^T$. Now, the boundary conditions at $x_s = 0$ and $x_s = H_s$ can be defined as follows:

$$M(x_s)|_{x_s=0} = \frac{\partial^2 W_s(x_s)}{\partial x_s^2} \Big|_{x_s=0} = 0 \quad (\text{A3})$$

$$V_s(x_s)|_{x_s=0} - P_{ss} = 0 \Rightarrow \frac{\partial^3 W_s(x_s)}{\partial x_s^3} \Big|_{x_s=0} = -\frac{P_{ss}}{E_p I_p} \quad (\text{A4})$$

$$M(x_s)|_{x_s=H_s} = \frac{\partial^2 W_s(x_s)}{\partial x_s^2} \Big|_{x_s=H_s} = 0 \quad (\text{A5})$$

$$V_s(x_s)|_{x_s=H_s} = 0 \Rightarrow \frac{\partial^3 W_s(x_s)}{\partial x_s^3} \Big|_{x_s=H_s} = 0 \quad (\text{A6})$$

Substituting Equations (A2) in (A3)–(A6), the boundary conditions can be written in matrix form as follows:

$$\begin{Bmatrix} \frac{\partial^2 W_s(x_s)}{\partial x_s^2} \Big|_{x_s=0} \\ \frac{\partial^3 W_s(x_s)}{\partial x_s^3} \Big|_{x_s=0} \\ \frac{\partial^2 W_s(x_s)}{\partial x_s^2} \Big|_{x_s=H_s} \\ \frac{\partial^3 W_s(x_s)}{\partial x_s^3} \Big|_{x_s=H_s} \end{Bmatrix} = \underbrace{\begin{bmatrix} 0 & -\lambda_{ss}^2 & 0\lambda_{ss}^2 \\ -\lambda_{ss}^3 & 0\lambda_{ss}^3 & 0 \\ -\lambda_{ss}^2 \sin(\lambda_{ss} H_s) & -\lambda_{ss}^2 \cos(\lambda_{ss} H_s) & \lambda_{ss}^2 \sinh(\lambda_{ss} H_s) & \lambda_{ss}^2 \cosh(\lambda_{ss} H_s) \\ -\lambda_{ss}^3 \cos(\lambda_{ss} H_s) & \lambda_{ss}^3 \sin(\lambda_{ss} H_s) & \lambda_{ss}^3 \cosh(\lambda_{ss} H_s) & \lambda_{ss}^3 \sinh(\lambda_{ss} H_s) \end{bmatrix}}_{\mathbf{Q}_s} \underbrace{\begin{Bmatrix} F_{s1} \\ F_{s2} \\ F_{s3} \\ F_{s4} \end{Bmatrix}}_{\mathbf{F}_s} = \underbrace{\begin{Bmatrix} 0 \\ -\frac{P_{ss}}{E_p I_p} \\ 0 \\ 0 \end{Bmatrix}}_{\mathbf{F}_{ss}} \quad (\text{A8})$$

$$\Rightarrow \mathbf{F}_s = \mathbf{Q}_s^{-1} \mathbf{F}_{ss}$$

Thus, substituting Equations (A8) in (A2), the closed-form expression of lateral spring stiffness can be obtained as follows:

$$K_L = \frac{P_{ss}}{W_s(x_s)|_{x_s=0}} = \frac{P_{ss}}{\mathbf{S}_s(x_s)|_{x_s=0} \mathbf{Q}_s^{-1} \mathbf{F}_s} \quad (\text{A9})$$

Appendix 2. Derivation for rotational spring stiffness

Thus, the boundary conditions at $x_s = H_s$ will be same as Equations (A3) and (A6). However, the boundary conditions

at $x_s = 0$ will be defined as follows:

$$M(x_s)|_{x_s=0} + M_{ss} = 0 \Rightarrow \frac{\partial^2 W_s(x_s)}{\partial x_s^2} \Big|_{x_s=0} = -\frac{M_{ss}}{E_p I_p} \quad (\text{A10})$$

and,

$$V_s(x_s)|_{x_s=0} = 0 \Rightarrow \frac{\partial^3 W_s(x_s)}{\partial x_s^3} \Big|_{x_s=0} = 0 \quad (\text{A11})$$

Substituting Equations (A2) in (A3), (A6), (A10), and (A11), the boundary conditions can be written in matrix form as follows:

$$\begin{Bmatrix} \frac{\partial^2 W_s(x_s)}{\partial x_s^2} \Big|_{x_s=0} \\ \frac{\partial^3 W_s(x_s)}{\partial x_s^3} \Big|_{x_s=0} \\ \frac{\partial^2 W_s(x_s)}{\partial x_s^2} \Big|_{x_s=H_s} \\ \frac{\partial^3 W_s(x_s)}{\partial x_s^3} \Big|_{x_s=H_s} \end{Bmatrix} = \mathbf{Q}_s \mathbf{F}_s = \underbrace{\begin{Bmatrix} -\frac{M_{ss}}{E_p I_p} \\ 0 \\ 0 \\ 0 \end{Bmatrix}}_{\mathbf{B}_{ss}} \Rightarrow \mathbf{F}_s = \mathbf{Q}_s^{-1} \mathbf{B}_{ss} \quad (\text{A12})$$

Thus, substituting Equations (A12) in (A2), the closed-form expression of rotational spring stiffness can be obtained as follows:

$$K_R = \frac{M_{ss}}{\theta_s(x_s)|_{x_s=0}} = \frac{M_{ss}}{\frac{\partial W_s(x_s)}{\partial x_s} \Big|_{x_s=0}} = \frac{M_{ss}}{\mathbf{T}_s(x_s)|_{x_s=0} \mathbf{Q}_s^{-1} \mathbf{B}_{ss}} \quad (\text{A13})$$

where $\mathbf{T}_s(x_s)|_{x_s=0} = \{\lambda_{ss} \ 0 \ \lambda_{ss} \ 0\}$.

Appendix 3. Derivation for equivalent stiffness

For a cantilever beam carrying a static load (P_s) at the free end, the governing differential equation defined in Equation (31) can be modified as follows:

$$\frac{\partial^2}{\partial \bar{x}^2} \left[(1 + \bar{c}\bar{x})^3 \frac{\partial^2 \bar{w}(\bar{x}, \bar{t})}{\partial \bar{x}^2} \right] = 0 \quad (\text{A14})$$

The exact solution for the above differential equation can be obtained as

$$\bar{w}(\bar{x}) = \bar{\Phi}(\bar{x}) \mathbf{E} \quad (\text{A15})$$

where, $\bar{\Phi}(\bar{x}) = \left\{ \frac{3+2(\bar{c}\bar{x}+1)\ln(\bar{c}\bar{x}+1)+2\bar{c}\bar{x}}{2\bar{c}^3(\bar{c}+1)} \ \frac{-\bar{c}}{2\bar{c}^3(\bar{c}+1)} \ \frac{\bar{c}\bar{x}+1}{\bar{c}+1} \ \frac{\bar{x}(\bar{c}\bar{x}+1)}{\bar{c}+1} \right\}$,

$\mathbf{E} = \{E_1 \ E_2 \ E_3 \ E_4\}^T$ and $\{\}^T$ is the transpose of a vector/matrix. Now, the non-dimensional boundary conditions as a function of $\bar{w}(\bar{x})$ at $\bar{x} = 0$ can be defined using Equation (33) as follows:

$$\bar{M}(\bar{x})|_{\bar{x}=0} = \frac{\partial^2 \bar{w}(\bar{x})}{\partial \bar{x}^2} \Big|_{\bar{x}=0} = 0 \quad (\text{A16})$$

and,

$$\begin{aligned} V_t(x)|_{x=0} - P_s &= 0 \Rightarrow \bar{V}(\bar{x})|_{\bar{x}=0} \\ &= \left(\eta_c(\bar{x}) \frac{\partial^2 \bar{w}(\bar{x})}{\partial \bar{x}^2} + \frac{\partial^3 \bar{w}(\bar{x})}{\partial \bar{x}^3} \right) \Big|_{\bar{x}=0} \\ &= \frac{\pi P_s E_t r_t^3 \tau}{H_t^3} \end{aligned} \quad (\text{A17})$$

Similarly, at $\bar{x} = 1$, the non-dimensional boundary conditions can be considered same as in Equations (35) and (36) as follows:

$$\begin{aligned} (\bar{M}(\bar{x}) + \kappa_R \bar{\theta}(\bar{x}))|_{\bar{x}=1} &\Rightarrow \frac{\partial^2 \bar{w}(\bar{x})}{\partial \bar{x}^2} \Big|_{\bar{x}=1} + \kappa_R \frac{\partial \bar{w}(\bar{x})}{\partial \bar{x}} \Big|_{\bar{x}=1} \\ &= 0 \end{aligned} \quad (\text{A18})$$

and,

$$\begin{aligned} (\bar{V}(\bar{x}) - \kappa_L \bar{w}(\bar{x}))|_{\bar{x}=1} &\Rightarrow \left(\eta_c(\bar{x}) \frac{\partial^2 \bar{w}(\bar{x})}{\partial \bar{x}^2} + \frac{\partial^3 \bar{w}(\bar{x})}{\partial \bar{x}^3} \right) \Big|_{\bar{x}=1} \\ &\quad - \kappa_L \bar{w}(\bar{x})|_{\bar{x}=1} \\ &= 0 \end{aligned} \quad (\text{A19})$$

Substituting Equations (A15) in (A16)–(A19), the boundary conditions can be written in matrix form as follows:

$$\begin{aligned} &\left\{ \begin{array}{l} \frac{\partial^2 \bar{w}(\bar{x})}{\partial \bar{x}^2} \Big|_{\bar{x}=0} \\ \left(\eta_c(\bar{x}) \frac{\partial^2 \bar{w}(\bar{x})}{\partial \bar{x}^2} + \frac{\partial^3 \bar{w}(\bar{x})}{\partial \bar{x}^3} \right) \Big|_{\bar{x}=0} \\ \frac{\partial^2 \bar{w}(\bar{x})}{\partial \bar{x}^2} \Big|_{\bar{x}=1} + \kappa_R \frac{\partial \bar{w}(\bar{x})}{\partial \bar{x}} \Big|_{\bar{x}=1} \\ \left(\eta_c(\bar{x}) \frac{\partial^2 \bar{w}(\bar{x})}{\partial \bar{x}^2} + \frac{\partial^3 \bar{w}(\bar{x})}{\partial \bar{x}^3} \right) \Big|_{\bar{x}=1} - \kappa_L \bar{w}(\bar{x})|_{\bar{x}=1} \end{array} \right\} \\ &= \left\{ \begin{array}{l} \frac{\partial^2 \bar{\phi}_i(\bar{x})}{\partial \bar{x}^2} \Big|_{\bar{x}=0} \\ \left(\eta_c(\bar{x}) \frac{\partial^2 \bar{\phi}_i(\bar{x})}{\partial \bar{x}^2} + \frac{\partial^3 \bar{\phi}_i(\bar{x})}{\partial \bar{x}^3} \right) \Big|_{\bar{x}=0} \\ \frac{\partial^2 \bar{\phi}_i(\bar{x})}{\partial \bar{x}^2} \Big|_{\bar{x}=1} + \kappa_R \frac{\partial \bar{\phi}_i(\bar{x})}{\partial \bar{x}} \Big|_{\bar{x}=1} \\ \left(\eta_c(\bar{x}) \frac{\partial^2 \bar{\phi}_i(\bar{x})}{\partial \bar{x}^2} + \frac{\partial^3 \bar{\phi}_i(\bar{x})}{\partial \bar{x}^3} \right) \Big|_{\bar{x}=1} - \kappa_L \bar{\phi}_i(\bar{x})|_{\bar{x}=1} \end{array} \right\} \underbrace{\begin{Bmatrix} E_1 \\ E_2 \\ E_3 \\ E_4 \end{Bmatrix}}_{\mathbf{E}} \\ &= \underbrace{\left\{ \begin{array}{l} 0 \\ \frac{\pi P E_t r_t^3 \tau}{L^3} \\ 0 \\ 0 \end{array} \right\}}_{\mathbf{J}} \end{aligned} \quad (\text{A20})$$

Here, i varies from 1 to 4. Thus, substituting Equations (A20) in (A15), the equivalent end stiffness can be obtained as

follows:

$$K_e = \frac{P_s}{\bar{w}(\bar{x})|_{\bar{x}=0}} = \frac{P_s}{\bar{\Phi}(\bar{x})|_{\bar{x}=0} \mathbf{Q}^{-1} \mathbf{J}} \quad (\text{A21})$$

Appendix 4. Derivation for equivalent mass

For a cantilever beam having a unit displacement amplitude at the free end of the beam, the non-dimensional boundary conditions as a function of $\bar{W}(\bar{x})$ at $x = 0$ and $x = H_t$ can be defined using Equations (33), (35) and (36) as follows:

$$\begin{aligned} \bar{W}(\bar{x})|_{\bar{x}=0} &= 1; \quad \frac{\partial^2 \bar{W}(\bar{x})}{\partial \bar{x}^2} \Big|_{\bar{x}=0} = 0; \\ \frac{\partial^2 \bar{W}(\bar{x})}{\partial \bar{x}^2} \Big|_{\bar{x}=1} + \kappa_R \frac{\partial \bar{W}(\bar{x})}{\partial \bar{x}} \Big|_{\bar{x}=1} &= 0 \end{aligned} \quad (\text{A22})$$

and,

$$\left(\eta_c(\bar{x}) \frac{\partial^2 \bar{W}(\bar{x})}{\partial \bar{x}^2} + \frac{\partial^3 \bar{W}(\bar{x})}{\partial \bar{x}^3} \right) \Big|_{\bar{x}=1} - \kappa_L \bar{W}(\bar{x})|_{\bar{x}=1} = 0 \quad (\text{A23})$$

A trial solution can be assumed for $\bar{W}(\bar{x})$ using the concept of static deflection as follows:

$$\bar{W}(\bar{x}) = L_1 + \bar{x}L_2 + \bar{x}^2L_3 + \bar{x}^3L_4 = \mathbf{ZL} \quad (\text{A24})$$

where, $\mathbf{Z} = \{1 \quad \bar{x} \quad \bar{x}^2 \quad \bar{x}^3\}$ and $\mathbf{L} = \{L_1 \quad L_2 \quad L_3 \quad L_4\}^T$. Thus, substituting Equations (A24) in (A22) and (A23), the boundary conditions can be written in matrix form as follows:

$$\begin{aligned} &\underbrace{\begin{bmatrix} 0 & 0 & 2 & 0 \\ 1 & 0 & 0 & 0 \\ 0 & 0 & 2 + 2\kappa_R & 6 + 6\kappa_R \\ -\kappa_L & -\kappa_L & \frac{6\bar{c}}{1+\bar{c}} - \kappa_L & \frac{18\bar{c}}{1+\bar{c}} + 6 - \kappa_L \end{bmatrix}}_{\mathbf{N}} \underbrace{\begin{Bmatrix} L_1 \\ L_2 \\ L_3 \\ L_4 \end{Bmatrix}}_{\mathbf{L}} \\ &= \underbrace{\begin{Bmatrix} 0 \\ 1 \\ 0 \\ 0 \end{Bmatrix}}_{\mathbf{I}} \Rightarrow \mathbf{L} = \mathbf{N}^{-1} \mathbf{I} \end{aligned} \quad (\text{A25})$$

Now, following Adhikari and Bhattacharya (2011), the kinetic energy (T_K) of the entire system can be defined as follows:

$$\begin{aligned} T_K &= \frac{1}{2} \int_0^{H_t} \left\{ \rho_t A_t(x) \left(\frac{\partial w_t(x, t)}{\partial t} \right)^2 \right\} dx \\ &\quad + \frac{1}{2} M_R \left(\frac{\partial w_t(x, t)}{\partial t} \Big|_{x=0} \right)^2 \\ &= -\frac{1}{2} \omega^2 e^{-2i\omega t} M_e \end{aligned} \quad (\text{A26})$$

where the equivalent mass (M_e) can be defined as follows:

$$M_e = \rho_t \int_0^L A_t(x) \mathbf{ZL}^T \mathbf{Z}^T dx + M_R \quad (\text{A27})$$